doi.org/10.26434/chemrxiv.9724061.v2

Operando Diffuse Reflectance UV-VIS Spectroelectrochemistry for Investigating Oxygen Evolution Electrocatalysts

Sebastian Wahl, Sayed M. El-Refaei, Patrick Amsalem, Ana de Oliveira Guilherme Buzanich, Norbert Koch, Nicola Pinna

Submitted date: 09/09/2019 • Posted date: 09/09/2019

Citation information: Wahl, Sebastian; El-Refaei, Sayed M.; Amsalem, Patrick; Buzanich, Ana de Oliveira Guilherme; Koch, Norbert; Pinna, Nicola (2019): Operando Diffuse Reflectance UV-VIS Spectroelectrochemistry for Investigating Oxygen Evolution Electrocatalysts. ChemRxiv. Preprint.

This is a complete self-standing study on operando diffuse reflectance UV-vis spectroelectrochemistry for investigating oxygen evolution electrocatalysts.

File list (2)

20190909-operando-JACS-submitted.pdf (1.79 MiB)	view on ChemRxiv • download file
20190909-operando-SI-JACS-submitted.pdf (1.97 MiB)	view on ChemRxiv • download file

Operando diffuse reflectance UV-Vis spectroelectrochemistry for investigating oxygen evolution electrocatalysts

Sebastian Wahl,[a] Sayed M. El-Refaei,[a] Patrick Amsalem,[b] Ana Guilherme Buzanich,[c] Norbert, Koch,[b] and Nicola Pinna*[a]

Affiliation

[a] Institut für Chemie and IRIS Adlershof, Humboldt-Universität zu Berlin, Brook-Taylor-Straße 2, 12489 Berlin, Germany,

[b] Institut für Physik and IRIS Adlershof, Humboldt-Universität zu Berlin, Brook-Taylor-Straße 6, 12489 Berlin, Germany,

[c] Bundesanstalt für Materialforschung und -prüfung (BAM), Richard-Willstätter-Straße 11, 12489 Berlin, Germany

Abstract

The characterization of the active structure of water splitting catalysts is crucial to evolve to a sustainable energy future based on hydrogen. Such an information can only be obtained by *operando* methods. We present a diffuse reflectance UV-Vis (DRUV) spectroelectrochemical study that allows to track the changes of solid oxygen evolution catalysts under working conditions. The versatility of our approach is demonstrated on two cobalt-containing catalysts $Zn_{0.35}Co_{0.65}O$ and $CoAl_2O_4$. The changes the catalysts undergo during the oxygen evolution reaction can be tracked by probing the electronic structure by UV-Vis spectroscopy. These findings are compared to *ex situ* analyses, which support the assignments of the structures stabilized under different potentials. Thus, structure-activity correlations can be proposed, and deeper insights into the catalytically active structures can be obtained.

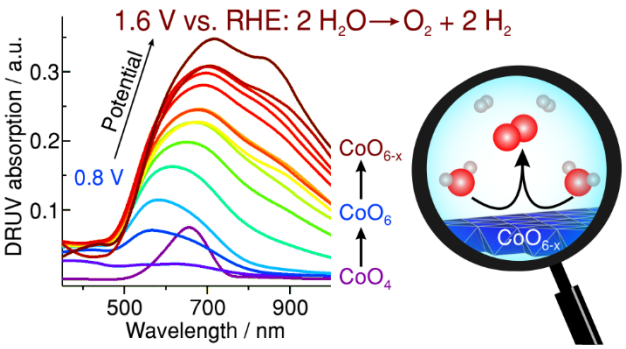

Introduction

For the development of earth-abundant catalysts for the oxygen evolution reaction (OER) that lay the basis for a sustainable energy future based on hydrogen from water, it is crucial to understand their active structure and the involved reaction mechanisms.[1] Therefore, adequate methods are needed to study catalysts under working conditions, i.e. *operando*. One suitable method is spectroelectrochemistry, which combines spectroscopy with electrochemical

measurements.[2] Recent developments focused mainly on *operando* X-ray absorption spectroscopy (XAS), which is a technique able to investigate the local structure of materials or molecules.[3-6] However, this technique requires extensive access to synchrotron facilities when dynamic processes or *operando* approaches need to be investigated. In addition, only a few working groups offer this possibility.

Another upcoming technique is *operando* X-ray photoelectron spectroscopy (XPS).[7] However, this technique is mainly limited to low pressure ranges. But there is more than just X-ray based methods. Spectroelectrochemistry was used first in the 1960s in combination with UV-visible absorption.[8] It allows to sensitively probe the electronic structure of samples. Beside the most common measurement in transmission geometry, where either a solution or a transparent substrate is needed, also reflection geometry can be utilized.[9-10] By diffuse reflectance UV-vis (DRUV) spectroscopy, solids can be analyzed, independent of their thickness or the substrate on which they are applied.[11] Various spectroelectrochemical cell (SEC) designs with different electrodes have been proposed and are commercially available.[12-19]

But to our best knowledge, nobody presented a DRUV approach yet to investigate catalysts under OER conditions. Therefore, we herein present an *operando* DRUV spectroelectrochemical study of cobalt containing catalysts.

To demonstrate the usability of *operando* DRUV, we performed experiments on two cobalt-containing model catalysts $Zn_{0.35}Co_{0.65}O$ and $CoAl_2O_4$, both starting with Co in a tetrahedral oxygen coordination. Therefore, a new spectroelectrochemical flow cell was developed, allowing the measurement on an existing spectrophotometer equipped with an integration sphere. The *ex situ* characterization of $Zn_{0.35}Co_{0.65}O$ was recently published by our group, and first structure-activity properties were proposed.[20] $CoAl_2O_4$ has been studied elsewhere for its optical properties as well as towards the OER. [5, 21-22] Herein, we performed detailed *ex situ* characterization of the material before and after electrochemical OER by high resolution transmission electron microscopy (HRTEM), powder X-ray diffraction (pXRD), X-ray photoelectron spectroscopy (XPS), and XAS. Furthermore, we are in the position to propose clear structure-activity correlations by evaluating the DRUV *operando* measurements in respect to the *ex situ* findings. We prove that our spectroelectrochemistry approach is able to provide insights on active phase catalysts under working conditions while requiring comparatively low resources.

Results

Dry measurements of $Zn_{0.35}Co_{0.65}O$

In our previous paper, it was demonstrated how the structure of $Zn_{0.35}Co_{0.65}O$ transforms under the influence of an alkaline milieu as well as of an applied potential to promote the oxygen evolution reaction (OER).[20] To get deeper understanding into the formation of the active oxygen evolution catalyst (OEC), *operando* DRUV spectroscopic measurements were performed, to connect the gained insights from *ex situ* analyses with the obtained spectra. The evolution of the spectra with applied potential can be found in **Fig. 1**.

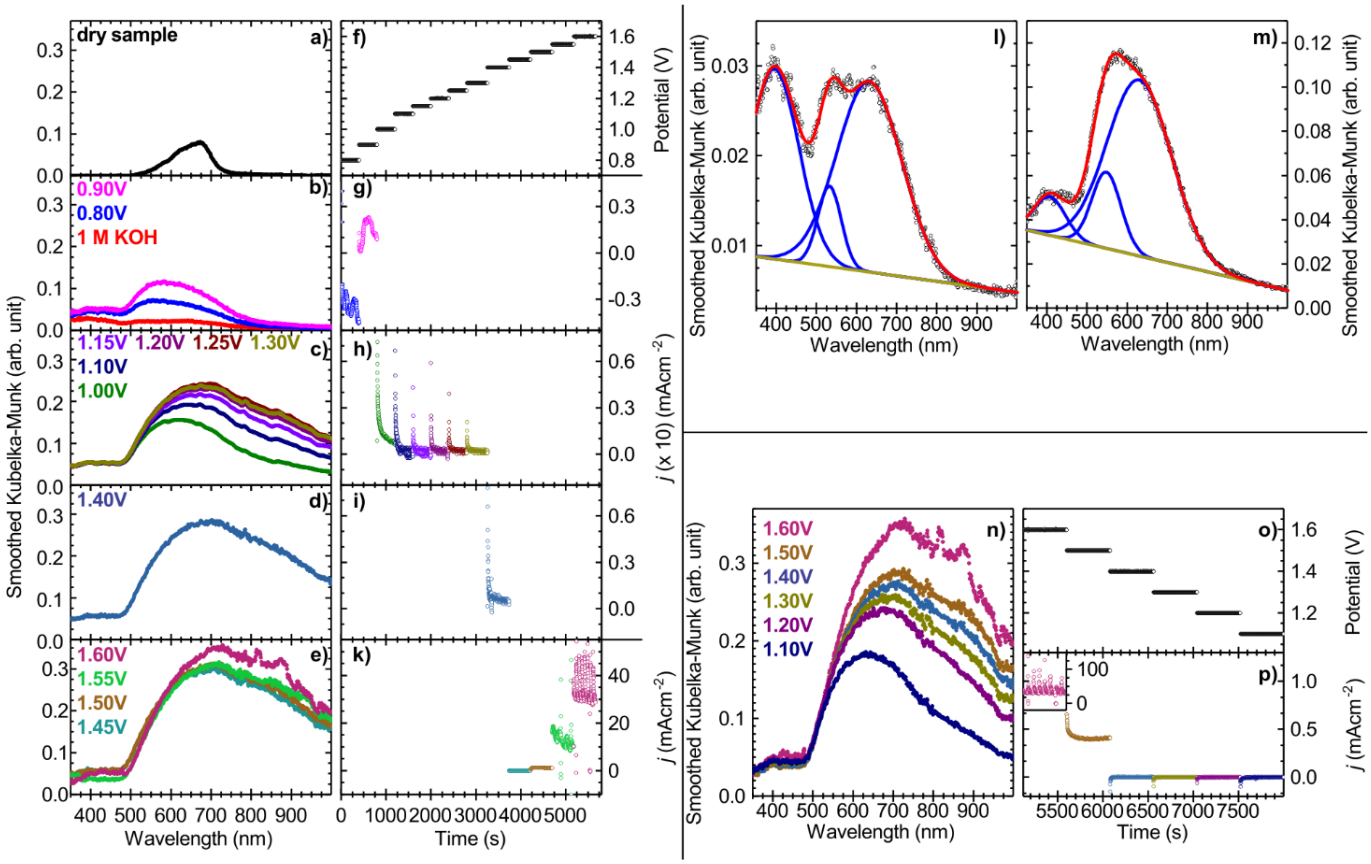

Figure 1. *Operando* DRUV spectroelectrochemistry of $Zn_{0.35}Co_{0.65}O$. a) DRUV spectrum of the dry sample on the SPE. b)-e) Spectra of the oxidation in 1 M KOH. f) Applied potential vs RHE as variation of time. g)-k) Corresponding current densities. The colors correspond to the applied potentials. l) Enlarged spectrum in 1 M KOH without applied potential. m) Enlarged spectrum at 0.9 V vs RHE. n) Spectra of the reduction in 1 M KOH. o) Applied potentials vs RHE as variation of time. p) Corresponding current densities. The inset in p) shows the current density at 1.6 V.

The spectrum of the dry sample in the cell (**Fig. 1a**) shows the typical Co^{2+}_{Td} (Td, tetrahedrally coordinated by four oxygen atoms) transitions at 667, 624 and 580 nm, which are based on a d^7 electron configuration and can be assigned to the transitions $^4A_2(F) \rightarrow {}^2E(G)$, $^4A_2(F) \rightarrow {}^4T_1(P)$ and $^4A_2(F) \rightarrow {}^2A_1(G)$, respectively.[23] In comparison to the measurement on the SPE outside the SEC (**Fig. S1**), the overall intensity is decreased, but the transitions are at the same positions.

$Zn_{0.35}Co_{0.65}O$ in 1 M KOH

Upon wetting the sample with 1 M KOH, the electronic transitions of Co^{2+}_{Td} vanish. The DRUV spectrum in 1 M KOH (**Fig. 1b** and **l** for more details) has a weak intensity compared to the spectra with an applied voltage. A deconvolution of the absorption bands below 800 nm yielded 3 underlying bands. As only a ligand exchange with OH^- and no oxidation of Co^{2+} is expected, a d^7 electron configuration should still be valid. Indeed, when using a d^7 electron configuration in a weak octahedral field, the first band centered at 632 nm falls in the region of the spin-allowed transition $^4T_{1g}(F) \rightarrow {}^4A_{2g}(F)$. Since this band was reported to be of little intensity, it might be as well arising from the splitting of ^2G free ion term.[24] It is followed by the likewise allowed transition $^4T_{1g}(F) \rightarrow {}^4T_{1g}(P)$ at 533 nm. At 396 nm and below that, bands arising from the splitting of the ^2H free ion term and the mixing with other states are expected.[25] Compared to the spectra of rock salt CoO nanoparticles (**Fig. S2b**), which also contain Co^{2+}_{Oh} (Oh, octahedrally coordinated by six oxygen atoms), the approximated Δ_O value is larger (8428 cm^{-1} vs 7326 cm^{-1}). This can be expected, as from the spectrochemical series the OH^--ligand is a σ-donor ligand and thus induces a stronger ligand field splitting than the oxo-ligand (O^{2-}), which has more of a π-donor character.[26] Therefore, the *in situ* spectrum of $Zn_{0.35}Co_{0.65}O$ in 1 M KOH can be assigned to Co^{2+}_{Oh}. These findings are supported by the *ex situ* pXRD pattern of $Zn_{0.35}Co_{0.65}O$ in 1 M KOH, which could be assigned to a $Co(OH)_2$ phase after the sample came in contact with KOH (**Fig. 1** in Reference 20). Thus, also the previously proposed formation mechanism of the OER catalyst via a brucite-type $Co(OH)_2$ intermediate can be confirmed.[20]

$Zn_{0.35}Co_{0.65}O$ at 0.9 V vs RHE

When a potential of 0.9 V is applied, only very little current is measured by chronoamperometry (CA, **Fig. 1g**). Therefore, again no change in oxidation state is expected (see also the cyclic voltammograms (CV) in Reference 20). The overall intensity is increased and the relative intensities of the absorption peaks change compared to the spectrum recorded without applied potential (**Fig. 1b** and **m** for more details). The maxima of the assigned transitions are close to the previously found. While the first two transitions at 630 nm and 548 nm show no difference in relative intensity, the one at 407 nm has a much lower relative intensity. The overall increase in intensity can be understood from the observation that by inducing a positive charge on the sample, Zn^{2+} ions leach from the structure by coulomb repulsion.[20] Thus, more defects are generated in the sample, which increases the mixing with transitions arising from lower symmetries than O_h, e.g. C_3 or D_{3d} (e.g. those are expected upon stretching or shrinking of an octahedron) leading to an increased absorption.[25, 27] Furthermore, the increase could be also due to spin-orbit coupling originating in the ^2G free ion terms.[24]

$Zn_{0.35}Co_{0.65}O$ at 1.3 V vs RHE

For the absorption spectra between 1.0 V and 1.3 V in **Fig. 1c**, obvious changes are visible in comparison to the spectrum recorded at 0.9 V. Those changes take place between 1.0 V and 1.2 V and indicate a change in the electronic structure of the sample. Between 1.2 V and 1.3 V, the spectra overlap, indicating the same electronic structure. In the spectra, the intensity raises with increasing potential, and the maximum absorption is shifted to lower energies (1.0 V: 620 nm, 1.1 V: 640 nm, 1.15 V: 650 nm, 1.2-1.3 V: 670 nm). Especially at higher wavelengths the increased absorption is noticeable. According to previous studies, the formation mechanism of an OEC from $Co(OH)_2$ involves the oxidation of Co^{2+} to Co^{3+} and further to Co^{4+}.[3, 28] The oxidation of Co^{2+} to Co^{3+} is expected between 1.0 and 1.2 V, which is in line with the observed changes in the spectra. Indeed, also the corresponding CA measurements show a current increase (**Fig. 1h**). The current density profiles especially at 1.0 V and 1.1 V point to a Faradaic current, which can be attributed to the oxidation of Co^{2+} to Co^{3+}. Integration of the current from 1.00 V to 1.20 V, where the changes in the spectra occur, gives a charge of 1.25 mC, which can be correlated to the initial sample loading of the catalyst to access the number of oxidized Co^{2+}. Consequently, around 15 % of the contained Co^{2+} is oxidized (see supporting information for further details). This is further in good agreement with the integration of the $Co^{2+/3+}$ oxidation peak of the first CV cycle of $Zn_{0.35}Co_{0.65}O$ (**Fig. 5a** in Ref. 20), which yielded that ~19 % of the contained Co^{2+} is oxidized to Co^{3+}. From this electrochemical analysis it can be concluded that a significant amount of Co^{2+} is still present in the sample. This further means that the recorded spectra are a superposition of spectra of Co^{2+} and Co^{3+} containing structures. According to the literature, the Co^{3+} containing phase prior to the OER consists of Co(O)OH units.[29-31] Thus, it is valid to assume that the structural units formed in our experiments are also Co(O)OH and are the origin of the observed absorption at higher wavelengths. However, when we compare the *operando* spectrum to the spectra of other d^6 reference materials such as Co(O)OH and $ZnCo_2O_4$ (**Fig. S3**), large differences are visible. In Co(O)OH reference hexagonal platelets (cf. Figure SI-5 in reference 18), the first absorption covers the region between 200 and 800 nm and no absorptions are recorded between 800 nm and 1100 nm. At lower energy, a very weak $^1A_{1g}(I) \rightarrow {}^3T_{1g}(H)$ transition can be observed (ca. 1250 nm). The spectrum of $ZnCo_2O_4$, in which only $Co^{3+}{}_{Oh}$ is expected, shows also an absorption minimum at around 1000 nm. In the *operando* spectrum, on the other hand, the onset of the first band lies at around 500 nm and strong absorptions are also observed between 800 and 1400 nm in the NIR region (**Fig. 1c** and **S4a**). When applying the Tanabe-Sugano theory for octahedral symmetry with a d^6 electron configuration in a strong ligand field, within reasonable values for B and Δ_O no bands are expected above 850 nm as the spectra of the reference materials show (**Fig. S3**). On the other

hand, the spectrum of $Zn_{0.35}Co_{0.65}O$ at 1.3 V shows a broad absorption between 500 and 1400 nm and thus it is reasonable to assume a lower symmetry than O_h. This assumption is further supported by the *ex situ* EXAFS measurements that showed a cobalt coordination number of 5.6 in the *in-situ* formed γ-Co(O)OH.[20] Since one metal center can only hold a natural number of ligands, a linear combination of sixfold and five- or less-coordinated Co should give a good approximation. Extreme cases of five-coordinated Co would be a square pyramid with C_{4v} geometry or a trigonal bipyramidal structure with D_{3h} geometry.[32-34] The continuous absorption above 700 nm can be further attributed to electrochromism. Electrochromism is ascribed to the oxidation of the central ion and subsequent intercalation of OH^- ions into the material to maintain electroneutrality under an anodic potential.[35-37] Thus, cobalt containing materials, namely Co_3O_4, are colored, i.e. increased absorption, upon anodic potential and bleached under cathodic potential.[38-41] Therefore, electrochromism causes a change of the band structure and of the geometry around the central ion. The Fermi-level is lowered, and thus electrons can get easier excited to the conduction band.

$Zn_{0.35}Co_{0.65}O$ at 1.4 V vs RHE

The CA shows Faradaic current when the potential is increased to 1.4V (**Fig. 1i**), which can be attributed to the oxidation of Co^{3+} to Co^{4+}, as also depicted by the shoulder in the CV (Fig. 5a in Ref. 20). When integrating the current (assuming no contributions of the OER), a charge of 0.62 mC is obtained. Comparing this value to the one obtained for the redox couple $Co^{2+/3+}$, roughly 50 % of Co^{3+} are further oxidized to Co^{4+}. The contribution of Co^{4+} to the spectrum can be seen in an increased absorption intensity in **Fig. 1d** and the shift of the absorption maximum to lower energies (690 nm). The observed increase of absorption at higher wavelengths is further in accordance to measurements done by Webster et al. for molecular $Co^{4+}{}_{Oh}$ species.[42] Contrary to those findings, the missing absorption at lower wavelengths points again to a deviation from O_h symmetry.

$Zn_{0.35}Co_{0.65}O$ at OER potential

From an applied potential of 1.45 V, the current shows no more decreasing when the potential is raised. Indeed, the observed stationary current can be attributed to the evolution of O_2. At 1.55 V, a current density of 10 $mAcm^{-2}$ is reached. The CA in **Fig. 1k** shows oscillations, which can be ascribed to the evolution of bubbles on the electrode and the inhibited mass transport of electrolyte to the electrode surface. The results are also clearly visible in the spectra in **Fig. 1e**. Especially in the lower energy regime, the noise increases more than for the previous measurements. The absorption maximum is further shifted to lower energies (1.45 V: 700 nm,

1.6 V: 720 nm), and the intensity is slightly increased. This indicates that during the ongoing OER more Co^{3+} is oxidized to Co^{4+}. The general shape of the absorption band is not changed, and thus also major deviations from a Co(O)OH structure are not expected between 1.4 V and OER potential. To validate the measurements, the *operando* spectra were also measured for the Co(O)OH reference hexagonal platelets (**Fig. S5**). The spectra show the same electrochromism and also the same trend in the shift of absorption maxima. This further proves that the Co(O)OH reference phase shows a similar behavior as our *in-situ* formed γ-Co(O)OH, that is, due to its layered structure large parts of the surface are involved in the water oxidation process.

$Zn_{0.35}Co_{0.65}O$ reduction

When reducing the potential to 1.1 V, the reversed effect as for the oxidation can be observed in **Fig. 1n-p**. The CAs from 1.4 to 1.1 V show a small negative current, which indicates the reduction of the Co^{4+} species. In the spectra, the intensity decreases with every potential decrease and the absorption maximum is shifted to higher energies (1.1 V: 630 nm). **Figure S4b** shows almost overlapping between the spectra recorded at 1.3 V under anodic and cathodic potential. The absorption intensity of the spectrum after the OER is slightly higher, but the maximum absorption is at the same value (673 nm). This proves that the geometrical and electronic structure changes under OER conditions are reversible.

Characterization of $CoAl_2O_4$

After measuring the optical response of a structure that is known to change its phase during the reaction, another structure was studied. $CoAl_2O_4$ in the spinel structure was synthesized by the “benzyl alcohol route”. This was achieved by using cobalt(II) acetate and aluminum triisopropoxide as metal precursors and benzyl alcohol as oxygen source, solvent and surface stabilizing agent.[22, 43-44] After 48 h at 250 °C in a PTFE-lined steel autoclave, the sample was washed with ethanol, solid products were collected by centrifugation and the sample was dried overnight at 70 °C. A blue powdered product was obtained.

The crystal structure of $CoAl_2O_4$ was identified by pXRD. Only typical reflections of the cubic spinel structure (ICSD PDF-number 01-070-0753)[45] were present in the pattern in **Fig. 2a**. Using the Scherrer equation, a mean crystallite size of 5.6 nm was calculated.

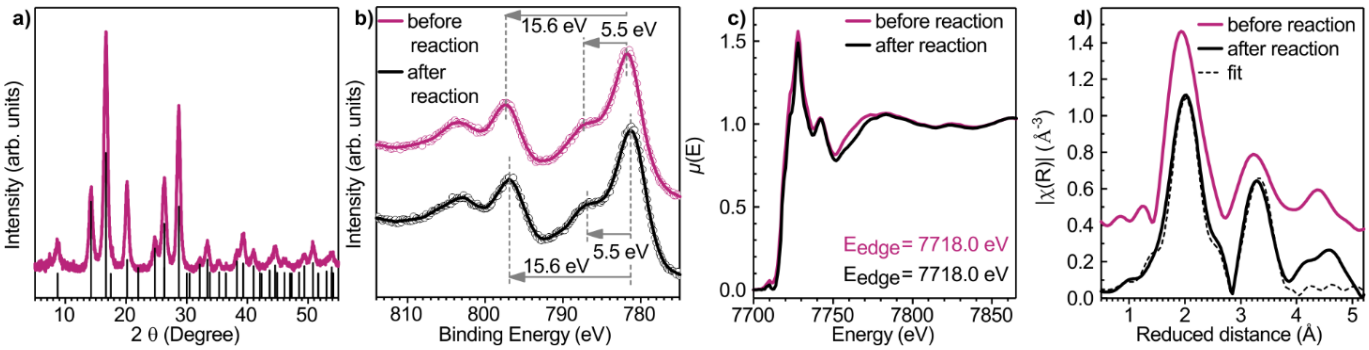

Figure 2. X-ray analyses on $CoAl_2O_4$. a) XRD pattern of $CoAl_2O_4$. Reference given is ICSD PDF-number 01-070-0753.[45] b) XPS spectra of $CoAl_2O_4$ before and after the reaction on the Co-edge. The peak positions and relative energy shifts point to an oxidation state of +II, before and after the reaction. c) XANES spectra of $CoAl_2O_4$ before and after reaction. d) Magnitude of the Fourier transforms of the recorded spectra of $CoAl_2O_4$ before and after reaction (*k*-range: 3.2–11.0). A fit was only possible for the latter.

Insight in the oxidation state of $CoAl_2O_4$ was gained by characterizing the chemical surface of the sample by XPS (**Fig. 2b**). The $Co2p_{3/2}$ peak is at 781.8 eV, with a shake-up satellite shifted by 5.5 eV. The $Co2p_{1/2}$ peak is shifted by 15.6 eV compared to $Co2p_{3/2}$. Compared to previous works, this indicates an oxidation state of +II for cobalt.[20, 46-47] The $Al2p_{3/2}$ peak (**Fig. S7a**) is at 74.1 eV, which points to Al^{3+} in an oxygen environment.[21] In the spectrum on the Al edge, some signal from gold is visible. This is due to bare gold electrode patches, on which the spectra were measured (see supporting information for more details).

HRTEM analyses of $CoAl_2O_4$ before the reaction in **Fig. 3a-c** show particles with a high crystallinity and with a mean size of 6.0 ± 1.4 nm, which is in good accordance to the crystallite size estimated by pXRD. The selected area electron diffractogram (SAED) shows the expected reflections of the $CoAl_2O_4$ phase with 311 as the most intense reflection (**Fig. 3b**).

Energy dispersive X-ray spectroscopic (EDX) analyses (see **Table 1**) yield a cobalt to aluminum ratio of 35.2 % to 64.8 % for $CoAl_2O_4$, confirming the expected stoichiometry of both metals in the material. The EDX mapping in **Fig. S9** shows the uniform distribution of the metals in the material.

Table 1. EDX analysis of $CoAl_2O_4$ before and after electrochemical reaction.

	Co atom%	***Al atom%***
Before reaction	35.2	64.8
After reaction	40.0	60.0

The DRUV spectrum in **Fig. S2a** shows the typical absorptions for Co^{2+}_{Td} at 634, 577 and 549 nm, which can be assigned to the transitions $^4A_2(F) \rightarrow {}^2E(G)$, $^4A_2(F) \rightarrow {}^4T_1(P)$ and $^4A_2(F) \rightarrow {}^2A_1(G)$, respectively.[23] The fine splitting of the transition $^4A_2(F) \rightarrow {}^4T_1(F)$ is visible

between 1800 to 1000 nm. At 1362 nm, the 2*v*(OH) harmonic band form residual surface OH-groups is observed.[48] Below 500 nm, a very strong absorption is visible, which could involve charge-transfer processes as well as transitions the free-ion ^{2}H term, which is split in the tetrahedral field.

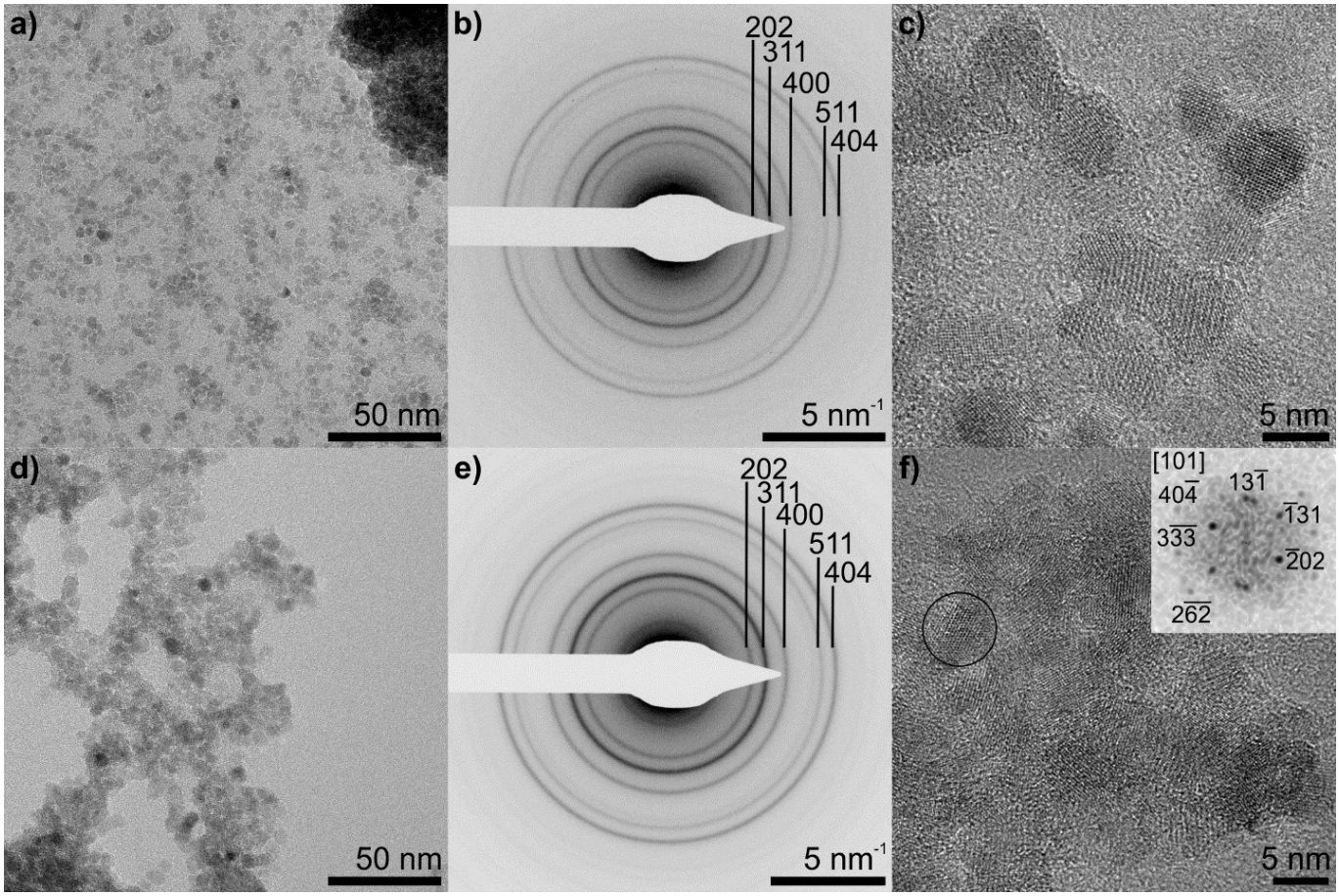

Figure 3. HRTEM micrographs of $CoAl_2O_4$ before (a-c) and after (d-f) 1 h electrochemical reaction at 10 mAcm^{-2}. a) and d) show an overview, b) and e) the SAED, with diffractions corresponding to spinel-type $CoAl_2O_4$. c) and f) show high resolution micrographs. The inset in f) shows the power spectrum of the marked area. The spots are assigned to the [101] zone axis of spinel-type $CoAl_2O_4$.

Electrocatalytic activity toward the OER was examined by rotating disk electrode (RDE) measurements in 1 M KOH. The CVs of $CoAl_2O_4$ at different scan rates are shown in **Fig. 4a**. The small anodic and cathodic peaks at ~1.06 V can be assigned to the redox-couple Co^{2+}/Co^{3+}. At ~1.43 V, peaks indicate the redox-pair Co^{3+}/Co^{4+}. The presence of anodic and cathodic peaks indicate a reversible reaction. At around 1.53 V, the onset of the OER starts.

From the power law relationship between the oxidation peak current (i) and the scan rate (v), $i=av^b$, it can be estimated, whether a surface or bulk redox process is taking place. *a* and *b* are adjustable parameters, and *b* can be expressed as the slope of the plot of log(*i*) vs log(*v*). When *b* is close to 0.5, a Faradaic redox process in the bulk is indicated, while *b* being close to 1.0 indicates a surface-limited redox process.[49-50] When fitting the slope of log(*i*) vs log(*v*) (**Fig. 4a**

inset), we obtain 0.9 as the *b* value for the redox-couple $Co^{2+/3+}$, indicating a surface-limited reaction for $CoAl_2O_4$.

The linear sweep voltammograms (LSV) in **Fig. 4b** shows the activity of $CoAl_2O_4$ compared to $Zn_{0.35}Co_{0.65}O$ and Co(O)OH. The overpotential towards the OER lies at 362 mV ($Zn_{0.35}Co_{0.65}O$: 322 mV, Co(O)OH: 382 mV) at a current density of 10 $mAcm^{-2}$ (averaged over three measurements). The electrochemically active surface area (ECSA) was determined from the double-layer capacitance according to McCrory et al. (**Fig. S8**).[51] It lies at 1.13 cm^2, and is thus smaller than the one of $Zn_{0.35}Co_{0.65}O$ (21.93 cm^2) and Co(O)OH (5.71 cm^2). The electrochemical performance is comparable to spinel type Co_3O_4.[20]

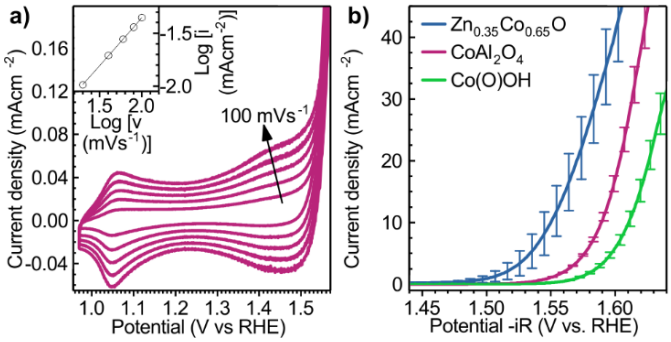

Figure 4. a) CVs of $CoAl_2O_4$ in 1 M KOH at different scan rates *v* (20, 40, 60, 80 and 100 mVs^{-1}). From these, the oxidation peak current *i* for the redox-couple $Co^{2+/3+}$ was determined. The inset shows log(*i*) vs log(*v*). The slope of the linear fit is 0.9. b) LSV of $Zn_{0.35}Co_{0.65}O$, $CoAl_2O_4$ and Co(O)OH in 1 M KOH. The error bars indicate the deviation of three measurements.

To analyze the influence of the OER on the material, it was held for 1 h at a current density of 10 $mAcm^{-2}$. In the XPS spectrum after the reaction in **Fig. 2b**, the $Co2p_{3/2}$ peak position is at 781.3 eV, and the shake-up satellite is shifted by ca. 5.5 eV. The $Co2p_{1/2}$ peak is shifted by 15.6 eV compared to $Co2p_{3/2}$. For Co^{3+} species the shake-up satellite is expected to be shifted by 10.0 eV compared to the $Co2p_{3/2}$.[46] Here, the markedly unchanged line shape of the Co2p spectrum after reaction points towards the same oxidation state as before reaction. The $Al2p_{3/2}$ peak (**Fig. S7a**) is shifted to 73.6 eV and can be assigned to Al^{3+} in an oxygen environment. The 0.5 eV energy shift of the Co and Al main peak positions can be attributed to small changes in the Fermi level of the thin films. This is further supported by the fact, that the oxygen main peak is shifted by the same amount (see **Fig. S7c**). From XPS it should be concluded that no major changes in oxidation state occur upon reaction.

The HRTEM micrographs after reaction in **Fig. 3d-e** show close aggregated particles. The SAED pattern in **Fig. 3e** shows one phase, that can be assigned to spinel-type $CoAl_2O_4$. Also the power spectral analysis indicates no second crystalline phase. On the other hand, as the

reflections of pure Co_3O_4 are expected at nearly the same position as for $CoAl_2O_4$, no distinction between those can be made.

The EDX analysis after the reaction (see **Table 1**) yields a cobalt to aluminum ratio of 40 % to 60 %, indicating a little loss of aluminum from the material.[52] The EDX mapping in **Fig. S10**, however, shows a uniform distribution of Co and Al in the particles. Following Lippens and Lannoo, for particles of 6.0 ± 1.4 nm size, 11 – 18 % of all atoms are located on the surface of a particle. Thus, the amount of Al leached can be attributed to the top most layer (see SI for details).[53]

Analysis of the X-ray absorption near-edge structure (XANES) spectra (**Fig. 2c**) shows no change in the edge energy (7718.0 eV) between $CoAl_2O_4$ before and after 1 h electrochemical reaction at 10 $mAcm^{-2}$. Also, in the fingerprint region after the edge, only little difference is visible. This is in accordance to the XPS results indicating no change in the oxidation state after the reaction.

Extended X-ray absorption fine structure (EXAFS) (**Fig. 2d**) of the sample before and after the reaction also shows high similarity. Unfortunately, the EXAFS before the reaction could not be fitted with just a simple model based on the crystal structure of $CoAl_2O_4$, probably due to the high surface to volume ratio in the small nanoparticles. A fit of the EXAFS after the reaction, however, was possible in the range from 1.15 to 3.6 Å, assuming a spinel unit cell without defects. The peak at a reduced distance of 2.00 Å corresponds to 4 oxygen atoms tetrahedrally coordinated around the central cobalt atom. The second shell is composed of 12 aluminum atoms in a reduced distance of 3.29 Å, 12 oxygen atoms at 3.33 Å and 4 cobalt atoms at 3.44 Å. The other fitting parameters can be found in **Table S9**. From comparison to the fit after reaction and with Maurizio et al.,[54] a qualitative analysis of the spectrum before the reaction can be done. The first peak must be from the oxygen coordinated around the cobalt atom. The second peak is less pronounced and a bit broader then after reaction, indicating less regular features that dissolve during the reaction. The third peak is at around the same position as after the reaction, but shows no shoulder. All in all, the EXAFS analysis of the samples also show no significant change in the main features after the reaction.

To conclude, the *ex situ* characterization of $CoAl_2O_4$ before and after the reaction indicate no significant change in the main crystalline structure. The loss of Al detected by EDX can be ascribed to the top-most surface layer of the nanoparticles, but an additional change in the surface structure could not be detected by our experiments.

Operando measurement of $CoAl_2O_4$

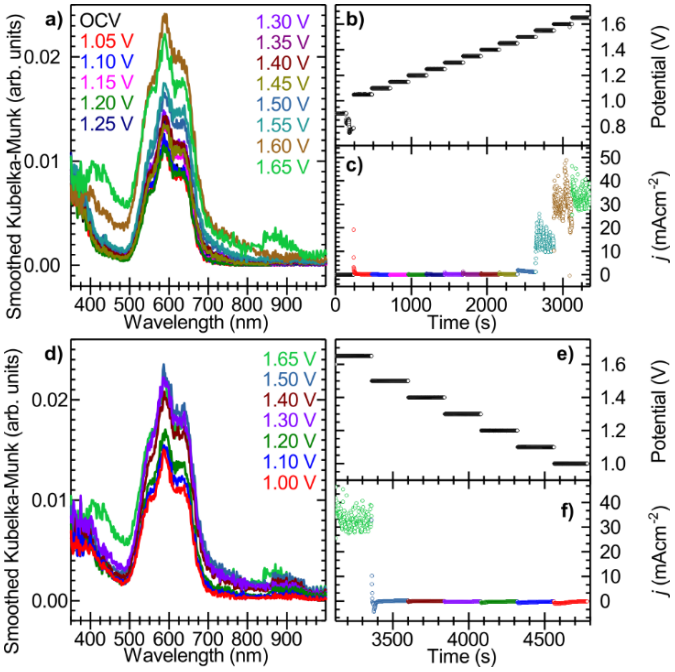

Figure 5: *Operando* DRUV spectroelectrochemistry of $CoAl_2O_4$. a) and d) DRUV spectra in 1 M KOH for oxidation and reduction, respectively, b) and e) Applied potentials, c) and f) Corresponding CA measurements.

$CoAl_2O_4$ nanoparticles were also measured by *operando* DRUV spectroscopy. In contrast to $Zn_{0.35}Co_{0.65}O$, where the sample undergoes phase transformations, here no significant changes in the structure could be observed after the OER. The spectra recorded under anodic potential in **Fig. 5a** show no shift in the peak positions compared to the spectrum of powdered $CoAl_2O_4$ nanoparticles (**Fig. S2a**), nor are there new bands visible. Only the intensity is slightly increased upon increasing potential. This can be again attributed to electrochromism. The increase of the bands below 500 nm, that are only present at high currents indicate the presence of another structural motif during the OER. The increased absorption above 800 nm at 1.65 V can be attributed to absorption of the gold substrate, which is only visible at high potentials (cf. **Fig. S6**). The noise in spectra at higher potentials is caused by the evolution of O_2 bubbles (cf. **Fig. 5 c** and **f**, indeed for applied potentials above 1.55 V the recorded current is above 10 mA/cm^{-2}). For the spectra recorded under cathodic potential (**Fig. 5d**), a decrease in the intensity can be observed. These spectra prove on the one hand that the “bulk” of the material (even though the particle size is below 10 nm) is unaffected under anodic potential, where the oxidation of cobalt to +IV species is expected. This is in line with the CV analysis, which points to redox reactions confined at the top most surface of the nanoparticles.[50] On the other hand it shows that the structures present under OER conditions are formed reversible. Additional structural characterizations before and after electrochemistry support our conclusions. As a matter of fact, SAEDs are unchanged (cf. **Fig. 3 b** and **e**) and no additional phases could be detected.

Moreover, STEM EDX mapping shows no change in the Al and Co distribution over the nanoparticles. On the other hand, a slight decrease of the Al concentration is recorded (few atom%, **Table 1**), pointing to the partial leaching of Al at the top most surface of the nanoparticles leading to reorganization of the surface. All in all, the *ex situ* structural and chemical characterizations match the *operando* DRUV studies and demonstrate that only the first atomic layers of the $CoAl_2O_4$ nanoparticles are active towards the OER, while the tetrahedral backbone of the material is still intact.

Discussion

The use of *operando* DRUV spectroscopy, together with our newly developed electrochemical flow cell, appears to be well suitable for the study of changes in the local structure of electrocatalysts under working conditions. Indeed, the *operando* measurements permitted to accurately follow the structural changes the $Zn_{0.35}Co_{0.65}O$ precatalyst undergoes, i.e. when it gets in contact with KOH and when a potential is applied. The observations in low potential regions could be analyzed and the results could be correlated to *ex situ* measurements. Thus, deeper insights in the formation mechanism of the active cobalt species could be gained. From a pure tetrahedral coordination of Co^{2+} the whole Wurtzite-type $Zn_{0.35}Co_{0.65}O$ material underwent a structural change to an octahedral Co^{2+} coordination (i.e. $Co(OH)_2$), without changing its oxidation state. When an anodic potential is applied, the oxidation state of Co is partly changed to +III (above 1.1 V) and +IV (above 1.4 V). The oxidation is coupled to a decrease of the symmetry around the central ion. Furthermore, it could be shown that at the OER potential (i.e. > 1.5 V) a significant amount of Co^{3+} is still present as only little shift of the absorption maximum could be observed compared to lower anodic potential (e.g. 1.3 V). This is in good agreement with the literature and the proposed mechanism for the OER, where the active centers switch the oxidation state between +III and +IV and involve either oxygen vacancies or peroxide species.[3, 55-57] It was also shown, that the formation of the active structural motif is a reversible process, as the spectra after the cathodic potential did not differ essentially from the ones under anodic potential. Nevertheless, the results indicate that several Co species in different oxidation states are present simultaneously during the OER.

The spectra recorded at 1 V and above show the advantages of the *operando* DRUV technique. Since UV-Vis absorption spectroscopy probes the valence electrons, it is very sensitive to small changes in the electronic structure of a sample. In the case of $CoAl_2O_4$, even changes that are confined to the top most surface layer of the nanoparticles can be seen. On the other hand, the assignment of certain bands to structural motifs is extremely complex, as the spectra are a superposition of contributions of several structures. Additionally, the spectra of the single solid

structures further include also fine splitting of the electronic terms depending on the ligand field geometry.

It should also be pointed out that only few electrocatalytical materials involve a phase transformation over the whole structure during the OER. For most materials, only the surface shows catalytic activity. As an example for this, $CoAl_2O_4$ was used as a model catalyst. The electrochemical data exhibited a high activity towards the OER. On the one hand, the *operando* DRUV measurements were able to prove that the clear signature of the Co^{2+} ions in tetrahedral environment is unaffected by the OER. On the other hand, increases in intensity and the presence of bands at elevated potentials indicate different reversible structural motifs that are only present during the OER. *Ex situ* analyses of $CoAl_2O_4$ further support these observations, as no change in the crystalline backbone could be seen and only changes on the top most surface were derived. From this, it is valid to assume that the catalytically active centers are on the top first atomic layers only. The inertia of the underlying tetrahedrally coordinated cobalt further indicates that the assignment of the active phase to one certain structure is not straightforward.

Interestingly, although the ECSA of $CoAl_2O_4$ is among the smallest of the studied systems, it has a significant activity towards the OER. This means it has a higher activity per center compared to the other materials studied, indicating that on these centers the structures for the OER are optimized. On the downside, fewer centers are available. Thus, new syntheses should strive to even smaller particles, to increase the number of active centers. Nevertheless, we showed that by combining DRUV measurements and *ex-situ* chemical and structural analyses, valuable information can be acquired even on materials bearing only surface catalytic species.

One of the advantages of the presented spectroelectrochemical technique lies in its wide accessibility when combined with the simple and inexpensive flow cell we have developed. Another advantage of the presented experimental setup is the modularity. The outlet of the cell can be coupled to a gas sensor, a mass spectrometer or another analysis technique to analyze the reaction products or dissolved species. By replacing the Quartz window with a Kapton™ foil, the setup can be applied in *operando* XAS measurements in fluorescence mode and in XRD in Bragg-Brentano geometry.

Conclusion

We propose the use of an *operando* DRUV spectroelectrochemical approach to follow changes in the electronic structure of oxygen evolution catalysts under working conditions. We successfully followed chemical and structural changes of two solid cobalt-based catalysts $Zn_{0.35}Co_{0.65}O$ and $CoAl_2O_4$ at OER potential and linked the results to *ex situ* characterizations. This allowed us to propose clear structure-activity correlations.

All in all, our approach bridges the gap between model catalysts studied by surface science techniques under UHV and catalyst materials studied under highly concentrated electrolytes and we are convinced that the electrocatalysis community will adopt it as a standard *operando* technique.

Experimental

Chemicals: All reagents were used as received. Cobalt(II) acetate (anhydrous, 98 %) was purchased from ABCR GmbH (Karlsruhe, Germany). Aluminum triisopropoxide (anhydrous, 98 %) and benzyl alcohol (puriss.) were purchased from Sigma Aldrich (Munich, Germany). Absolute ethanol (EMPARTA) was purchased from VWR International GmbH (Darmstadt, Germany). 1 N potassium hydroxide solution was purchased from Carl Roth GmbH (Karlsruhe, Germany).

Materials for the SEC: MetalVelvet™ black foil sheet, low outgassing adhesive (ACM Coatings GmbH, Naumburg, Germany). PEEK raw part (Grünberg Kunststoffe, Berlin, Germany). PTFE raw part (ADS Drehservice GmbH, Ahaus, Germany). Quartz glass cover slip, Ø18 mm, 0.25 mm thick (Plano GmbH, Wetzlar, Germany). Silicone sheet, white, 0.5 mm thick, ~60 Sh-A (Modulor GmbH, Berlin, Germany). To seal small leakings: One components silicone rubber Scrintec® 600, oxime cross-linking (Carl Roth GmbH,Karlsruhe, Germany). 0.8 mm diameter PTFE tubing, flanged (VWR International GmbH, Darmstadt, Germany).

Syntheses: Syntheses of $Zn_{0.35}Co_{0.65}O$, $ZnCo_2O_4$, Co(O)OH and CoO were described before.[20] $CoAl_2O_4$ was synthesized by adding cobalt(II) acetate (248 mg, 1.4 mmol, 1 eq.) and aluminium triisopropoxide (572 mg, 2 mmol, 2 eq.) to benzyl alcohol (25 mL) in a 45 mL PTFE-lined stainless steel autoclave (Parr Instruments GmbH, Frankfurt, Germany) equipped with a stirring bar in an argon atmosphere. After sealing the autoclave, it was placed on a stirring plate and stirred for 2 h to dissolve all solids. Then, it was heated at 250 °C for 48 h. After cooling, product was obtained as a blue dispersion. Collecting the solid product by centrifugation and washing with ethanol was challenging, as the dispersion formed in benzyl alcohol as well as in ethanol was very stable. After washing, the product was dried at 70°C in an oven. 185 mg of a blue product were obtained (74 % yield based on precursor's stoichiometry).

Flow cell design: The front part is made from polyether ether ketone (PEEK), which is covered with a black foil (MetalVelvet™, ACM Coatings GmbH) with a 4 mm hole, to only reflect light from the working electrode. The front is placed on a mount and hold by magnets at the reflectance port of the spectrophotometer. In the main area, the PEEK has a thickness of 2 mm. A 0.25 mm thick Quartz window is embedded in the PEEK and allows the light to pass to the working electrode and back. It also allows for measurements in the near-infrared (NIR) range. An SPE (DropSens 250AT, Metrohm) is used as the substrate for the catalyst and is connected via a 2 pin connector cable

(2.54 mm contact spacing) to the potentiostat. The catalyst is placed on the 4 mm Au electrode, and the Pt ring around acts as the counter electrode. The SPE is placed in silicone gaskets that direct the flow of the electrolyte. The front gasket is 0.5 mm thick and thus the volume in front of the electrode is ~50 µL. The total distance from the electrode to the reflectance port is only ~2.5 mm. The electrolyte passes through the channel in front of the electrode and the 2 mm diameter channels in the back part of the SEC, which is made from polytetrafluoroethylene (PTFE). It is connected by PTFE tubes with HPLC fittings to the peristaltic pump and the waste bottle. The electrolyte is pumped at a rate of 0.92 mL/min through the system and thus the solution in front of the electrode is renewed ~18 times per minute. The tip of the RHE reference electrode (Mini HydroFlex®, gaskatel) is in contact to the electrolyte in the inlet channel to allow for a controlled potential in the cell. Wing bolts and nuts tighten the setup. A 3D-printed cover with holes for the tubes, cables and RHE protects the cell from ambient light. Additionally, the system is covered with a black tissue. Blueprints are available upon request from the corresponding author. A scheme of the cell can be found in **Fig. S11**. Photographs are shown in **Fig. S12**.

Characterization: XRD diffraction patterns were obtained using a STOE STADI MP (STOE, Darmstadt, Germany) running at U = 50 kV and I = 40 mA with Mo Kα = 0.70930 Å) monochromatic radiation (using a Ge(111) monochromator) and a DECTRIS "MYTHEN 1K" detector. The patterns were recorded in *2 θ* geometry in the range of 4 to 60 °.

HRTEM images and EDX mappings were obtained using a FEI Talos F200S operated at 200 kV scanning/transmission electron microscope (S/TEM). Particle sizes were estimated by measuring 250 particles manually.

X-ray photoelectron spectroscopy (XPS) was performed in an ultrahigh vacuum chamber (base pressure 5.10-10 mbar) using a JEOL JPS-9030 set-up comprising a hemispherical photoelectron spectrometer and a monochromatic Al Kα (h*v* = 1486.6 eV) X-ray source. The XPS measurements were performed with an energy resolution of 1.25 eV as determined on a polycrystalline Ag *3d* core level. The samples were directly measured on SPEs. The spectra were corrected for charging by shifting the C1s peaks to 284.8 eV.

XANES and EXAFS measurements of the samples before electrochemical reaction were performed at the BAM*line* (BESSY-II, Helmholtz Centre Berlin for Materials and Energy Berlin, Germany). The beam was monochromatized using a double-crystal monochromator (DCM). The size of the beam was 3 x 1 mm. The measurements were performed at Co-K edge (7709 eV) in transmission geometry, with two ionization chambers as detectors. The excitation energy was varied from 7614 eV to 8428 eV, with varying energy steps. For the pre-edge region, the energy was varied in 10 eV steps; for the region around the edge, energy was tuned in 0.5 eV steps and in the EXAFS region with a constant step in the k-space of 0.04 $Å^{-1}$. The associated uncertainty was experimentally determined by measuring the cobalt metal foil 10 times. A value of ±0.3 eV was obtained. For the measurement, the samples were mixed with boron nitride and fixed in plastic sample holders. Before collecting the sample spectra, a cobalt foil was used as a reference for the cobalt edge. The relative energies of the spectra were calibrated to the first infliction point of the cobalt metal absorption edge. To determine the edge energy, the first infliction point was used. EXAFS data were processed by ATHENA and ARTEMIS from Demeter version 0.9.26.[58] This GUIs program belongs to the main package IFEFFIT (v. 1.2.12).[59]

Electrochemical analyses were performed using a Bio-Logic VMP3 multichannel potentiostat/ galvanostat with a built-in EIS analyzer. The electrochemical behavior and activity of catalysts were measured in a three-electrode

electrochemical cell using a 3 mm diameter glassy carbon rotating disc electrode (RDE, Autolab RRDE, Metrohm, Filderstadt, Germany) operated at 1600 rpm at 25 °C. A platinum wire was used as the counter electrode and a reversible hydrogen electrode (HydroFlex, gaskatel, Kassel, Germany) was used as a reference electrode. The electrodes were prepared by drop casting 3 µL of a catalyst ink onto glassy carbon. The ink was prepared by sonicating 1 mg catalyst powder with 490 µL ethanol, 490 µL purified water and 20 µL Nafion for 30 min.
The sample after reaction for the HRTEM and XAS analyses was prepared by dropcasting an ethanolic dispersion of the $CoAl_2O_4$ onto a nickel foil, performing 1 h chronopotentiometry at a current density of 10 $mAcm^{-2}$, rinsing the foil with ethanol and scratching off the material. This was repeated several times.

DRUV spectroscopy was performed on a PerkinElmer LAMBDA 950 UV/Vis Spectrophotometer equipped with a 150 mm integrating sphere. Powdered samples were measured at the reflectance sample holder port, by mixing them with a small amount of $BaSO_4$. Spectra were measured in the wavelength range between 2500 and 200 nm. For baseline detection, pure $BaSO_4$ was used, and the Kubelka-Munk function was used to compute the spectra.

Operando DRUV measurements were performed in the cell described above and in the predecessor model (supporting information and **Fig. S13**). A 4 mm gold screen-printed electrode (DropSens 250AT, Metrohm, Filderstadt, Germany). Screen-printed platinum was used as the counter electrode and a reversible hydrogen electrode (Mini HydroFlex®, gaskatel, Kassel, Germany) was used as the reference electrode. The cell was connected to a BioLogic SP50 portable single channel potentiostat / galvanostat. The cell was placed at the reflectance sample holder port of the above mentioned spectrophotometer, and covered with a 3D-printed cover and a black tissue. For baseline detection, a blank SPE was used. The samples were prepared by drop casting 2 µL of a catalyst ink on the Au electrode of the SPE. The catalyst ink was prepared by dispersing 5 mg of catalyst powder in 1 mL ethanol using an ultrasonic bath. The spectra were collected in the range between 1000 and 350 nm with a resolution of 1 nm. 1 M KOH was used as the electrolyte, and the flow was controlled to 0.92 mL/min by a tubing pump (flow rate 0.03 to 8.20 mL/min, neoLab Migge GmbH, Heidelberg, Germany). The spectra were measured 30 s after a new potential was applied, respectively. All spectra were exported as csv-files by the spectrometers software and treated further with OriginPro 2017. Spectra then were computed using the Kubelka-Munk function. The band positions were obtained manually by selecting the maximum intensity of a band or the position of a shoulder or by Gaussian peak deconvolution. The band positions then were compared to the corresponding online available Tanabe-Sugano diagram via a self-written Python 3 script, and the most probable transitions were assigned.[60] The most probable band assignment based on this method can be found in the supporting information for the spectra shown (**Table S1**-**S8**).

Acknowledgements

Special thanks to Bernd Lück, Sven Zillmann and Bettina Röder (workshops of HU Berlin and BAM) for design considerations and manufacturing the SEC. Thanks to Christoph Erdmann for measuring HRTEM and S/TEM. S.M.E. is grateful for Yousef Jameel Scholarship Fund. Special thanks to Fabian Müller and Patricia Russo for fruitful discussions.

Author contributions

S.W. and N.P. have designed the study, analyzed the data and wrote the paper. P.A. provided XPS measurements and analysis. S.M.E. provided electrochemical measurements. A.G.B. provided XAS measurements and guidance to the interpretation. N.K. contributed to the interpretation of the XPS results.

Competing interests: The authors declare no competing interests.

Keywords: operando • spectroelectrochemistry • DRUV • cobalt • structure-property relationships

1. United Nations Transforming our world: The 2030 agenda for sustainable development. *Resolution adopted by the General Assembly* **2015**.
2. Gale, R. J. *Spectroelectrochemistry: theory and practice*. Plenum Press, New York and London: 1988.
3. Bergmann, A.; Jones, T. E.; Moreno, E. M.; Teschner, D.; Chernev, P.; Gliech, M.; Reier, T.; Dau, H.; Strasser, P. Unified structural motifs of the catalytically active state of Co (oxyhydr) oxides during the electrochemical oxygen evolution reaction. *Nat. Catal.* **2018,** *1* (9), 711.
4. Menezes, P. W.; Indra, A.; Bergmann, A.; Chernev, P.; Walter, C.; Dau, H.; Strasser, P.; Driess, M. Uncovering the prominent role of metal ions in octahedral versus tetrahedral sites of cobalt–zinc oxide catalysts for efficient oxidation of water. *J. Mater. Chem. A* **2016,** *4* (25), 10014-10022.
5. Wang, H.-Y.; Hung, S.-F.; Chen, H.-Y.; Chan, T.-S.; Chen, H. M.; Liu, B. In operando identification of geometrical-site-dependent water oxidation activity of spinel Co3O4. *J. Am. Chem. Soc.* **2015,** *138* (1), 36-39.
6. Friebel, D.; Louie, M. W.; Bajdich, M.; Sanwald, K. E.; Cai, Y.; Wise, A. M.; Cheng, M.-J.; Sokaras, D.; Weng, T.-C.; Alonso-Mori, R.; Davis, R. C.; Bargar, J. R.; Nørskov, J. K.; Nilsson, A.; Bell, A. T. Identification of Highly Active Fe Sites in (Ni,Fe)OOH for Electrocatalytic Water Splitting. *J. Am. Chem. Soc.* **2015,** *137* (3), 1305-1313.
7. Zhang, X.; Chen, Y.-S.; Kamat, P. V.; Ptasinska, S. Probing Interfacial Electrochemistry on a Co3O4 Water Oxidation Catalyst Using Lab-Based Ambient Pressure X-ray Photoelectron Spectroscopy. *J. Phys. Chem. C* **2018,** *122* (25), 13894-13901.
8. Kuwana, T.; Darlington, R. K.; Leedy, D. W. Electrochemical Studies Using Conducting Glass Indicator Electrodes. *Anal. Chem.* **1964,** *36* (10), 2023-2025.
9. Takashima, T.; Ishikawa, K.; Irie, H. Detection of Intermediate Species in Oxygen Evolution on Hematite Electrodes Using Spectroelectrochemical Measurements. *J. Phys. Chem. C* **2016,** *120* (43), 24827-24834.
10. Takashima, T.; Yamaguchi, A.; Hashimoto, K.; Irie, H.; Nakamura, R. In situ UV-vis Absorption Spectra of Intermediate Species for Oxygen-Evolution Reaction on the Surface of MnO₂ in Neutral and Alkaline Media. *Electrochemistry* **2014,** *82* (5), 325-327.
11. Takamura, T.; Takamura, K.; Nippe, W.; Yeager, E. Specular Reflection Studies of Gold Electrodes in situ. *J. Electrochem. Soc.* **1970,** *117* (5), 626-630.
12. León, L.; Mozo, J. D. Designing spectroelectrochemical cells: A review. *TrAC, Trends Anal. Chem.* **2018,** *102*, 147-169.
13. Pine Research Instrumentation Honeycomb Spectroelectrochemical Cell Kit. https://pineresearch.com/shop/products/spectroelectrochemistry/honeycomb-cell-kit/honeycomb-spectroelectrochemical-cell-2/ (accessed June 11, 2019).

14. Metrohm DropSens product website. http://www.dropsens.com/en/screen_printed_electrodes_pag.html (accessed June 11, 2019).
15. Bio-Logic Science Instruments SpectroElectrochemistry. https://www.bio-logic.net/accessories/spectroelectrochemistry/?filter[division]=ec-lab (accessed June 11, 2019).
16. González-Diéguez, N.; Colina, A.; López-Palacios, J.; Heras, A. Spectroelectrochemistry at Screen-Printed Electrodes: Determination of Dopamine. *Anal. Chem.* **2012,** *84* (21), 9146-9153.
17. Thiyagarajan, N.; Chang, J.-L.; Senthilkumar, K.; Zen, J.-M. Disposable electrochemical sensors: A mini review. *Electrochem. Commun.* **2014,** *38*, 86-90.
18. Li, M.; Li, Y.-T.; Li, D.-W.; Long, Y.-T. Recent developments and applications of screen-printed electrodes in environmental assays—A review. *Anal. Chim. Acta* **2012,** *734*, 31-44.
19. redoxme A. B. Company website of redoxme AB. https://redox.me (accessed June 11, 2019).
20. Wahl, S.; El-Refaei, S. M.; Buzanich, A. G.; Amsalem, P.; Lee, K.-S.; Koch, N.; Doublet, M.-L.; Pinna, N. $Zn_{0.35}Co_{0.65}O$ – A Stable and Highly Active Oxygen Evolution Catalyst Formed by Zinc Leaching and Tetrahedral Coordinated Cobalt in Wurtzite Structure. *Adv. Energy Mater.* **2019,** *9*, 1900328.
21. Duan, X.; Pan, M.; Yu, F.; Yuan, D. Synthesis, structure and optical properties of CoAl2O4 spinel nanocrystals. *J. Alloys Compd.* **2011,** *509* (3), 1079-1083.
22. Karmaoui, M.; Silva, N. J.; Amaral, V. S.; Ibarra, A.; Millán, Á.; Palacio, F. Synthesis of cobalt aluminate nanopigments by a non-aqueous sol–gel route. *Nanoscale* **2013,** *5* (10), 4277-4283.
23. Weakliem, H. A. Optical spectra of Ni2+, Co2+, and Cu2+ in tetrahedral sites in crystals. *J. Chem. Phys.* **1962,** *36* (8), 2117-2140.
24. Lever, A. B. P. *Inorganic electronic spectroscopy / A.B.P. Lever*. 2nd ed. ed.; Elsevier: Amsterdam, Oxford, New York, Tokio, 1986.
25. Andrut, M.; Wildner, M. Superposition model analysis from polarized electronic absorption spectra of Co^{2+} in trigonally distorted octahedra in brucite-type Co(OH)_2. *Journal of Physics: Condensed Matter* **2001,** *13* (33), 7353-7353.
26. Figgis, B. N.; Hitchman, M. A. *Ligand Field Theory and Its Applications*. Wiley-VCH: 2000.
27. Rückamp, R.; Benckiser, E.; Haverkort, M. W.; Roth, H.; Lorenz, T.; Freimuth, A.; Jongen, L.; Möller, A.; Meyer, G. E. R. D.; Reutler, P.; others Optical study of orbital excitations in transition-metal oxides. *New Journal of Physics* **2005,** *7* (1), 144-144.
28. Gerken, J. B.; McAlpin, J. G.; Chen, J. Y. C.; Rigsby, M. L.; Casey, W. H.; Britt, R. D.; Stahl, S. S. Electrochemical Water Oxidation with Cobalt-Based Electrocatalysts from pH 0–14: The Thermodynamic Basis for Catalyst Structure, Stability, and Activity. *J. Am. Chem. Soc.* **2011,** *133* (36), 14431-14442.
29. Smith, R. D. L.; Prévot, M. S.; Fagan, R. D.; Trudel, S.; Berlinguette, C. P. Water Oxidation Catalysis: Electrocatalytic Response to Metal Stoichiometry in Amorphous Metal Oxide Films Containing Iron, Cobalt, and Nickel. *J. Am. Chem. Soc.* **2013,** *135* (31), 11580-11586.
30. Koza, J. A.; Hull, C. M.; Liu, Y.-C.; Switzer, J. A. Deposition of β-Co(OH)2 Films by Electrochemical Reduction of Tris(ethylenediamine)cobalt(III) in Alkaline Solution. *Chem. Mater.* **2013,** *25* (9), 1922-1926.
31. Burke, M. S.; Kast, M. G.; Trotochaud, L.; Smith, A. M.; Boettcher, S. W. Cobalt–iron (oxy) hydroxide oxygen evolution electrocatalysts: the role of structure and composition on activity, stability, and mechanism. *J. Am. Chem. Soc.* **2015,** *137* (10), 3638-3648.
32. Wood, J. S.; Greene, P. T. Ligand field theory for pentacoordinate molecules. II. Crystal field-spin-orbit coupling treatment of the d1, d3, d6, and d8 configurations in trigonal-bipyramidal molecules and the magnetic properties of E ground terms. *Inorg. Chem.* **1969,** *8* (3), 491-497.
33. Morassi, R.; Bertini, I.; Sacconi, L. Five-coordination in iron(II); cobalt(II) and nickel(II) complexes. *Coord. Chem. Rev.* **1973,** *11* (4), 343-402.
34. Zhilinskaya, V. V.; Kozlov, G. A.; Nazarenko, Y. P.; Yatsimirskii, K. B. Electronic absorption spectra of cobalt (III) pentacyanide complexes. *Theor. Exp. Chem.* **1981,** *16* (4), 402-406.

35. Gottesfeld, S.; McIntyre, J. D. E. Electrochromism in anodic iridium oxide films II. pH effects on corrosion stability and the mechanism of coloration and bleaching. *J. Electrochem. Soc.* **1979,** *126* (5), 742-750.
36. Gorenstein, A.; Da Fonseca, C. N. P.; Torresi, R. M. In *Electrochromism in cobalt oxyhydroxide thin films*, Optical Materials Technology for Energy Efficiency and Solar Energy Conversion X, 1991; pp 104-116.
37. Burke, L. D.; Lyons, M. E.; Murphy, O. J. Formation of hydrous oxide films on cobalt under potential cycling conditions. *Journal of Electroanalytical Chemistry and Interfacial Electrochemistry* **1982,** *132*, 247-261.
38. Burke, L. D.; Murphy, O. J. Electrochromic behaviour of oxide films grown on cobalt and manganese in base. *Journal of Electroanalytical Chemistry and Interfacial Electrochemistry* **1980,** *109* (1), 373-377.
39. Da Fonseca, C. N. P.; De Paoli, M.-A.; Gorenstein, A. The electrochromic effect in cobalt oxide thin films. *Adv. Mater.* **1991,** *3* (11), 553-555.
40. Patil, P. S.; Kadam, L. D.; Lokhande, C. D. Studies on electrochromism of spray pyrolyzed cobalt oxide thin films. *Sol. Energy Mater. Sol. Cells* **1998,** *53* (3), 229-234.
41. Yuan, Y. F.; Xia, X. H.; Wu, J. B.; Gui, J. S.; Chen, Y. B.; Guo, S. Y. Electrochromism in mesoporous nanowall cobalt oxide thin films prepared via lyotropic liquid crystal media with electrodeposition. *Journal of Membrane Science* **2010,** *364* (1-2), 298-303.
42. Webster, R. D.; Heath, G. A.; Bond, A. M. Voltammetric, EPR and UV-VIS-NIR spectroscopic studies associated with the characterisation of electrochemically generated tris (dithiocarbamato) cobalt (IV) complexes in dichloromethane. *J. Chem. Soc., Dalton Trans.* **2001,** (21), 3189-3195.
43. Pinna, N.; Niederberger, M. Surfactant-free nonaqueous synthesis of metal oxide nanostructures. *Angew. Chem. Int. Ed.* **2008,** *47* (29), 5292-5304.
44. Bilecka, I.; Djerdj, I.; Niederberger, M. One-minute synthesis of crystalline binary and ternary metal oxide nanoparticles. *Chem. Commun.* **2008,** (7), 886-888.
45. Toriumi, K.; Ozima, M.; Akaogi, M.; Saito, Y. Electron-density distribution in crystals of CoAl2O4. *Acta Crystallogr. B* **1978,** *34* (4), 1093-1096.
46. Yang, J.; Liu, H.; Martens, W. N.; Frost, R. L. Synthesis and characterization of cobalt hydroxide, cobalt oxyhydroxide, and cobalt oxide nanodiscs. *J. Phys. Chem. C* **2010,** *114* (1), 111-119.
47. Biesinger, M. C.; Payne, B. P.; Grosvenor, A. P.; Lau, L. W. M.; Gerson, A. R.; Smart, R. S. C. Resolving surface chemical states in XPS analysis of first row transition metals, oxides and hydroxides: Cr, Mn, Fe, Co and Ni. *Appl. Surf. Sci.* **2011,** *257* (7), 2717-2730.
48. Brik, Y.; Kacimi, M.; Ziyad, M.; Bozon-Verduraz, F. Titania-Supported Cobalt and Cobalt–Phosphorus Catalysts: Characterization and Performances in Ethane Oxidative Dehydrogenation. *J. Catal.* **2001,** *202* (1), 118-128.
49. Brezesinski, T.; Wang, J.; Polleux, J.; Dunn, B.; Tolbert, S. H. Templated Nanocrystal-Based Porous TiO2 Films for Next-Generation Electrochemical Capacitors. *J. Am. Chem. Soc.* **2009,** *131* (5), 1802-1809.
50. Wang, H.-Y.; Hung, S.-F.; Hsu, Y.-Y.; Zhang, L.; Miao, J.; Chan, T.-S.; Xiong, Q.; Liu, B. In Situ Spectroscopic Identification of μ-OO Bridging on Spinel Co3O4 Water Oxidation Electrocatalyst. *J. Phys. Chem. Lett.* **2016,** *7* (23), 4847-4853.
51. McCrory, C. C. L.; Jung, S.; Peters, J. C.; Jaramillo, T. F. Benchmarking heterogeneous electrocatalysts for the oxygen evolution reaction. *J. Am. Chem. Soc.* **2013,** *135* (45), 16977-16987.
52. Zhang, J.; Klasky, M.; Letellier, B. C. The aluminum chemistry and corrosion in alkaline solutions. *J. Nucl. Mater.* **2009,** *384* (2), 175-189.
53. Lippens, P. E.; Lannoo, M. Calculation of the band gap for small CdS and ZnS crystallites. *Physical review. B, Condensed matter* **1989,** *39* (15), 10935-10942.
54. Maurizio, C.; El Habra, N.; Rossetto, G.; Merlini, M.; Cattaruzza, E.; Pandolfo, L.; Casarin, M. XAS and GIXRD Study of Co Sites in CoAl2O4 Layers Grown by MOCVD. *Chem. Mater.* **2010,** *22* (5), 1933-1942.

55. Zhang, M.; De Respinis, M.; Frei, H. Time-resolved observations of water oxidation intermediates on a cobalt oxide nanoparticle catalyst. *Nat. Chem.* **2014,** *6* (4), 362.
56. Favaro, M.; Yang, J.; Nappini, S.; Magnano, E.; Toma, F. M.; Crumlin, E. J.; Yano, J.; Sharp, I. D. Understanding the oxygen evolution reaction mechanism on CoO x using operando ambient-pressure X-ray photoelectron spectroscopy. *J. Am. Chem. Soc.* **2017,** *139* (26), 8960-8970.
57. Huang, Z.-F.; Song, J.; Du, Y.; Xi, S.; Dou, S.; Nsanzimana, J. M. V.; Wang, C.; Xu, Z. J.; Wang, X. Chemical and structural origin of lattice oxygen oxidation in Co–Zn oxyhydroxide oxygen evolution electrocatalysts. *Nature Energy* **2019,** *4* (4), 329-338.
58. Ravel, B.; Newville, M. ATHENA, ARTEMIS, HEPHAESTUS: data analysis for X-ray absorption spectroscopy using IFEFFIT. *J. Synchrotron Radiat* **2005,** *12* (4), 537-541.
59. Newville, M. IFEFFIT : interactive XAFS analysis and FEFF fitting. *J. Synchrotron Radiat* **2001,** *8* (2), 322-324.
60. Lancashire, R. J. Tanabe-Sugano diagrams via spreadsheets. http://wwwchem.uwimona.edu.jm/courses/Tanabe-Sugano/TSspread.html (accessed May 13, 2019).

Supporting Information

Operando diffuse reflectance UV-Vis spectroelectrochemistry for investigating oxygen evolution electrocatalysts

Additional DRUV spectra

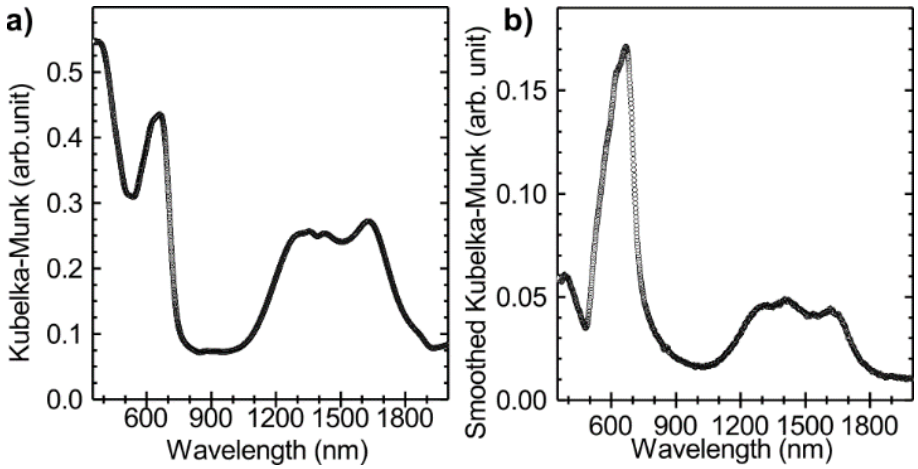

Figure S1. DRUV spectra of powdered $Zn_{0.35}Co_{0.65}O$ a) with $BaSO_4$ background and b) on Au working electrode of an SPE with the bare electrode as background.

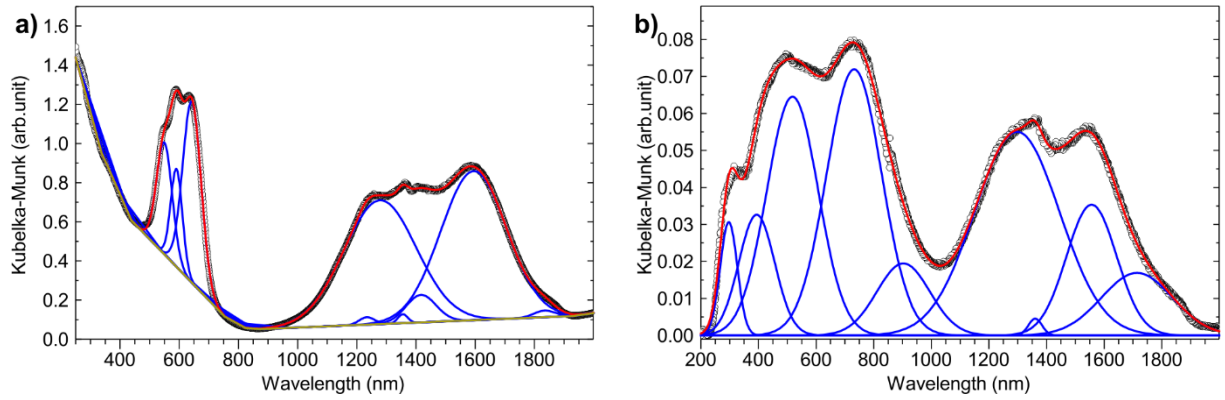

Figure S2. DRUV spectra of a) powdered $CoAl_2O_4$ nanoparticles and b) powdered CoO nanoparticles in rock salt structure as a reference for Co^{2+}_{oh}.

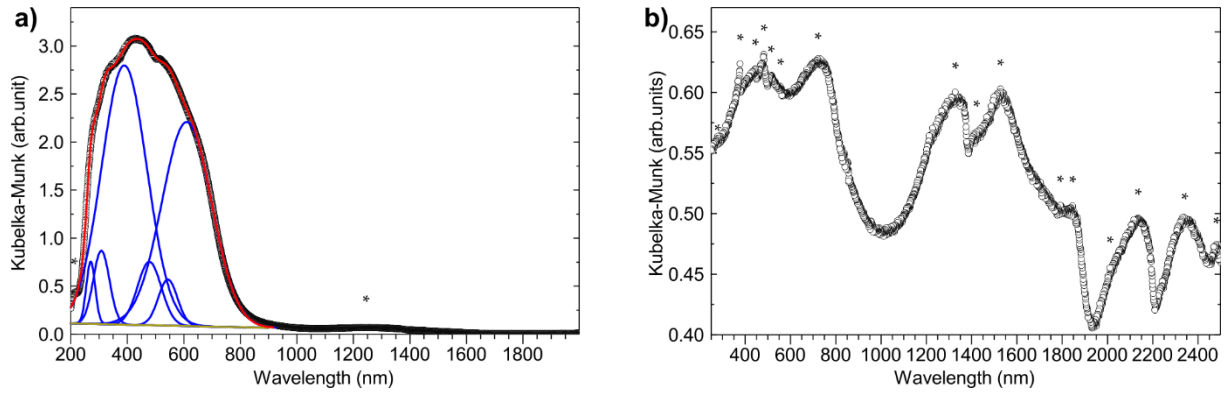

Figure S3. DRUV spectrum of a) powdered Co(O)OH nanoparticles and b) powdered $ZnCo_2O_4$ nanoparticles as references for Co^{3+}_{oh}. Asterisks mark peak positions not fitted.

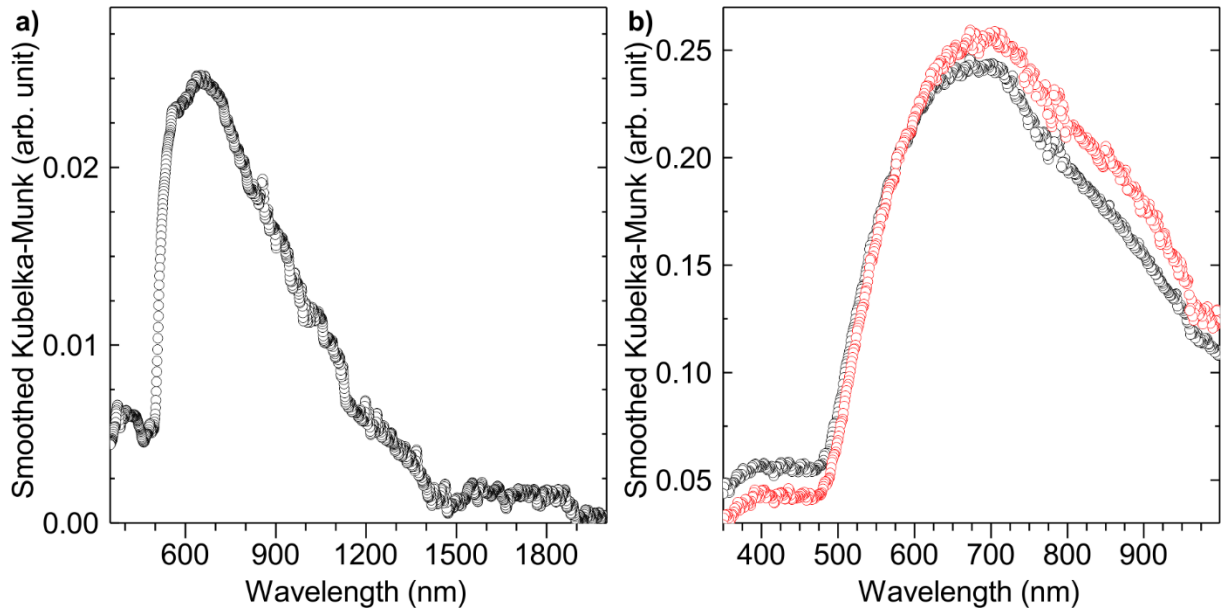

Figure S4. a) *Operando* DRUV spectrum of $Zn_{0.35}Co_{0.65}O$ at 1.3 V vs RHE showing also the NIR range. b) *Operando* DRUV spectra of $Zn_{0.35}Co_{0.65}O$ at 1.3 V vs RHE at oxidation (black) and reduction (red).

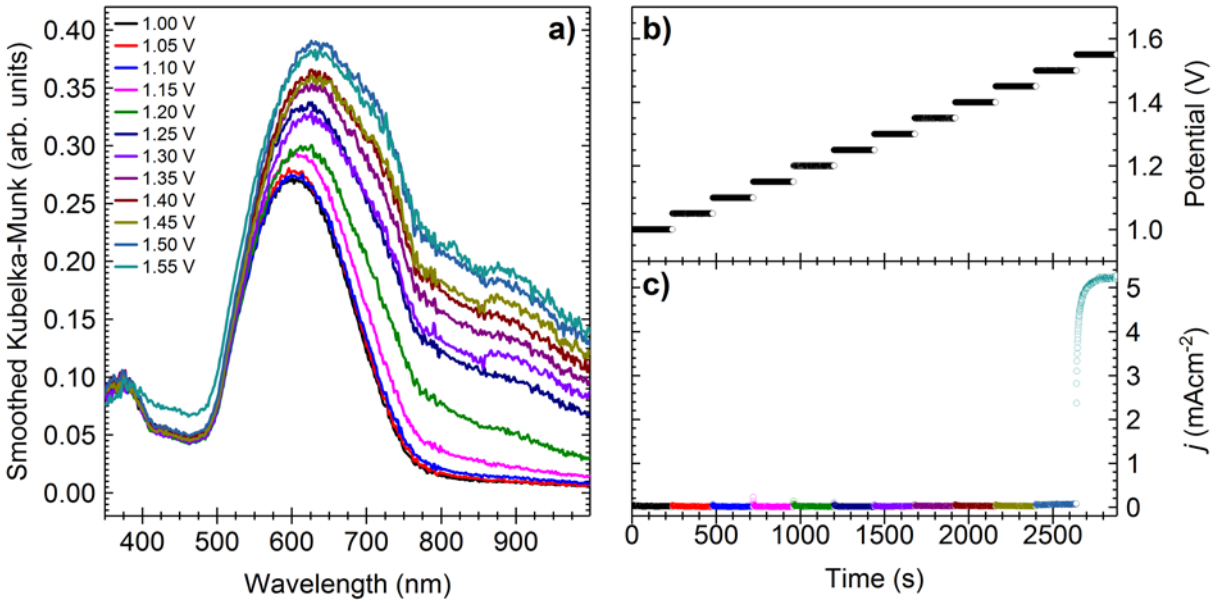

Figure S5. *Operando* DRUV spectroelectrochemistry of Co(O)OH nanoparticles. a) DRUV spectra of Co(O)OH in 1 M KOH, b) potential as a variation of time, c) CA measurements show the current density as a function of time. The colors correspond to the potential.

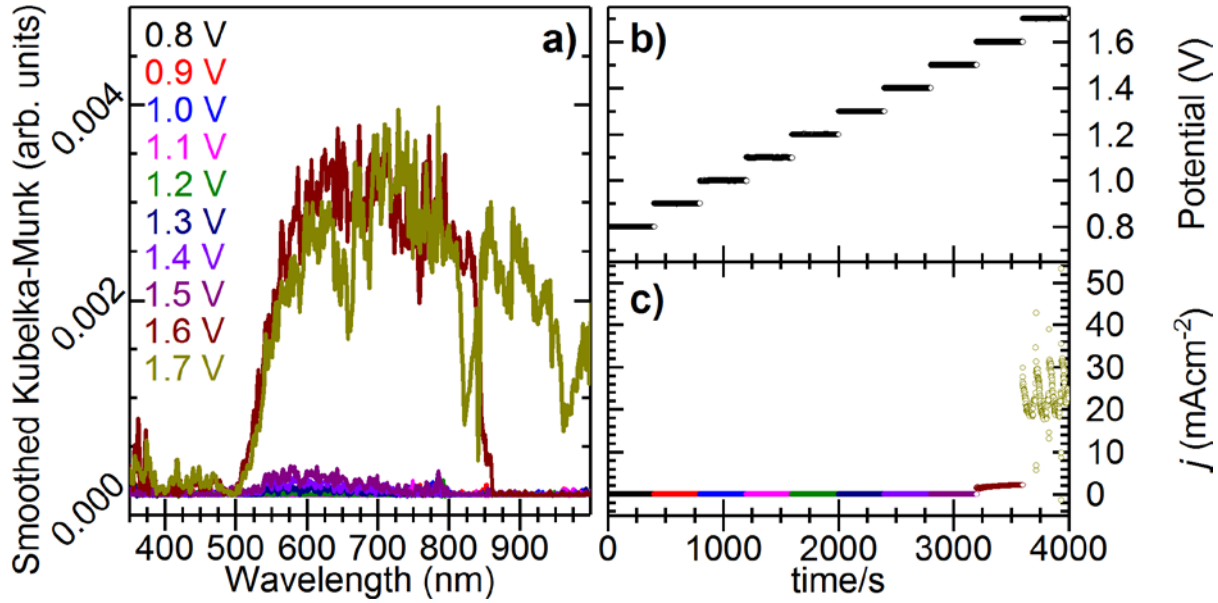

Figure S6. *Operando* DRUV spectroelectrochemistry of the SPE without loading as the control. a) DRUV spectra of SPE 250AT in 1 M KOH, b) potential as a variation of time, c) CA measurements show the current density as a function of time. The colors correspond to the potential.

Calculating the amount of Co oxidized during the operando measurement

The integration of the current in a CA measurement gives access to the charge transferred during the chosen time interval. Assuming all current is Faradaic, integrating the current for the time the spectra changed in **Fig. 1c** and **h**, i.e. between 1.0 V and 1.2 V, a charge of 1.25 mC is obtained. By division by the Faraday constant (96485 C/mol), the amount of transferred electrons is 0.0130 µmol. This charge can now be correlated to the initial sample loading, which was 10 µg (2 µL of catalyst ink (5 mg/mL) on the SPE). The estimated molar mass of $Zn_{0.35}Co_{0.65}O$ is 77.19 g/mol, and thus the loading on the SPE was 0.130 µmol of catalyst or 0.084 µmol of Co. Thus, 15.4 % of all initially contained Co^{2+} atoms are oxidized during this time.

When integrating the oxidation peak of the $Co^{2+/3+}$ redox couple in the first CV cycle of $Zn_{0.35}Co_{0.65}O$ (**Fig. 5a** in Reference 20, scan rate: 20 mV/s), a charge of 0.45 mC is obtained. The initial loading of catalyst was 3 µg (3 µL catalyst ink (1 mg/mL) on glassy carbon), which equals 0.039 µmol catalyst or 0.025 µmol Co. Correlating the charge to the initial loading, 18.5 % of all contained Co^{2+} atoms are oxidized in the first CV cycle. This is in good agreement of the value obtained from the *operando* measurement. However, this analysis does not take into account cobalt species dissolved during the measurement.

Integration of the current at 1.4 V, where the oxidation $Co^{3+/4+}$ is expected and the contribution of the OER should be still very small, yields a charge of 0.62 µC. Calculating the ratio between Co^{4+}/Co^{3+}, a value of 49.8 % is obtained. Thus, half of the contained Co^{3+} is oxidized to Co^{4+}.

DRUV band assignments

In the following tables, bands were assigned to transitions predicted by the according Tanabe-Sugano diagrams taken from R.J. Lancashire.[1] Bands written in parentheses were assigned to the nearest transition based on the approximated values for B and Δ/B, but need to be treated with caution. In the last column, the expected positions of the assigned bands are given, based on the according Tanabe-Sugano diagram. The band positions are obtained manually by selecting the maximum intensity of a band or the position of a shoulder or by Gaussian peak deconvolution.

Table S1. Band positions and assignment for DRUV spectrum of powdered $CoAl_2O_4$ nanoparticles in **Figure S1a**. The bands are assigned assuming tetrahedral Co^{2+} (d^7). Transitions are derived from Tanabe-Sugano diagram for d^3 octahedral (approximated values: B = 806 cm^{-1}, Δ/B = 4.9).

Wavelength	**Wavenumber**	**assigned transition**	**expected at**
[/nm]	[/cm^{-1}]		[/nm]
1854 1585 1405 1257	5394 6309 7117 7955	fine structure of $^4A_2(F) \rightarrow {}^4T_1(F)$	1458
1362	7342	2v(OH) harmonic band	
634	15 773	$^4A_2(F) \rightarrow {}^2E(G)$	631
577	17 007	$^4A_2(F) \rightarrow {}^4T_1(P)$	585
549	18 215	$^4A_2(F) \rightarrow {}^2A_1(G)$	553
< 500	> 20000	unassigned transitions	

Table S2. Band positions and assignment for DRUV spectrum of powdered CoO nanoparticles in **Figure S1b**. The bands are assigned assuming octahedral Co^{2+} (d^7) in a weak field. Transitions are derived from Tanabe-Sugano diagram for d^7 octahedral (approximated values: B = 933 cm^{-1}, Δ/B = 7.9).

Wavelength	**Wavenumber**	**assigned transition**	**expected at**
[/nm]	[/cm^{-1}]		[/nm]
1714 1556 1297	5835 6425 7708	fine structure of $^4T_{1g}(F) \rightarrow {}^4T_{2g}(F)$	1582
1360	7351	2v(OH) harmonic band	
903	11078	not assigned	
732	13658	$^4T_{1g}(F) \rightarrow {}^4A_{2g}(F)$	732
518	19301	$^4T_{1g}(F) \rightarrow {}^4T_{1g}(P)$	518
394	25394	$(^4T_{1g}(F) \rightarrow {}^2T_{2g}(H))$	387
297	33682	$(^4T_{1g}(F) \rightarrow {}^2E_g(D))$	305

Table S3. Band positions and assignment for DRUV spectrum of powdered Co(O)OH nanoparticles in **Figure S2a**. The bands are assigned assuming octahedral Co^{3+} (d^6) in a strong field. Transitions are derived from Tanabe-Sugano diagram for d^6 octahedral (approximated values: B = 777 cm^{-1}, Δ/B = 23.7).

Wavelength	Wavenumber	assigned transition	expected at
[/nm]	[/cm^{-1}]		[/nm]
1244	8039	$^1A_{1g}(I) \rightarrow {}^3T_{1g}(H)$	1118
610	16393	$^1A_{1g}(I) \rightarrow {}^1T_{1g}(I)$	610
544 478	18382 20921	(splitting of $^1T_{1g}(I)$ state)	
389	25707	$^1A_{1g}(I) \rightarrow {}^1T_{2g}(I)$	389
308	32468	($^1A_{1g}(I) \rightarrow {}^3T_{2g}(G)$)	311
271	36900	(splitting of free-ion ^1G state)	
213	46948	($^1A_{1g}(I) \rightarrow {}^3T_{1g}(G)$)	212

Table S4. Band positions and assignment for DRUV spectrum of powdered $ZnCo_2O_4$ nanoparticles in **Figure S2b**. The bands are assigned assuming octahedral Co^{3+} (d^6) in a strong field. Transitions are derived from Tanabe-Sugano diagram for d^6 octahedral (approximated values: B = 661 cm^{-1}, Δ/B = 23.6).

Wavelength	Wavenumber	assigned transition	expected at
[/nm]	[/cm^{-1}]		[/nm]
2482 2341 2136 2011	4029 4272 4682 4973	Unassigned	
1845 1791 1527 1422	5420 5583 6549 7032	(fine structure of $^1A_{1g}(I) \rightarrow {}^5T_{2g}(D)$)	1567
1327	7536	$^1A_{1g}(I) \rightarrow {}^3T_{1g}(H)$	1327
721	13870	$^1A_{1g}(I) \rightarrow {}^1T_{1g}(I)$	721
555 514 483 444 377 281	18018 19455 20747 22523 26525 35587	fine structure of $^1A_{1g}(I) \rightarrow {}^1T_{2g}(I)$ and higher transitions	459

Table S5. Band positions and assignment for DRUV spectrum of powdered $Zn_{0.35}Co_{0.65}O$ nanoparticles with $BaSO_4$ background in **Figure 2a**. The bands are assigned assuming tetrahedral Co^{2+} (d^7). Transitions are derived from Tanabe-Sugano diagram for d^3 octahedral (approximated values: B = 776 cm^{-1}, Δ/B = 4.6).

Wavelength	Wavenumber	assigned transition	expected at
[/nm]	[/cm^{-1}]		[/nm]
1867 1629 1426 1325	5356 6139 7013 7547	fine structure of $^4A_2(F) \rightarrow {}^4T_1(F)$	1596
1355	7380	2v(OH) harmonic band	1567
661	15129	$^4A_2(F) \rightarrow {}^2E(G)$	657
622	16077	$^4A_2(F) \rightarrow {}^4T_1(P)$	618

575	17391	$^4A_2(F) \rightarrow {}^2A_1(G)$	582
377	26525	$(^4A_2(F) \rightarrow {}^2E(D))$	372

Table S6. Band positions and assignment for DRUV spectrum of $Zn_{0.35}Co_{0.65}O$ on SPE in **Figure 2b**. The bands are assigned assuming tetrahedral Co^{2+} (d^7). Transitions are derived from Tanabe-Sugano diagram for d^3 octahedral (approximated values: B = 768 cm^{-1}, Δ/B = 4.7).

Wavelength	**Wavenumber**	**assigned transition**	**expected at**
[/nm]	[/cm^{-1}]		[/nm]
1615 1535 1409 1310	6192 6515 7097 7634	fine structure of $^4A_2(F) \rightarrow {}^4T_1(F)$	1580
667	14993	$^4A_2(F) \rightarrow {}^2E(G)$	664
624	16026	$^4A_2(F) \rightarrow {}^4T_1(P)$	621
580	17241	$^4A_2(F) \rightarrow {}^2A_1(G)$	586
382	26178	$(^4A_2(F) \rightarrow {}^2E(D))$	373

Table S7. Band positions and assignment for DRUV spectrum of $Zn_{0.35}Co_{0.65}O$ on SPE in 1 M KOH in **Figure 4a**. The bands are assigned assuming octahedral Co^{2+} (d^7). Transitions are derived from Tanabe-Sugano diagram for d^7 octahedral (approximated values: B = 827 cm^{-1}, Δ/B = 10.2).

Wavelength	**Wavenumber**	**assigned transition**	**expected at**
[/nm]	[/cm^{-1}]		[/nm]
632	15823	$(^4T_{1g}(F) \rightarrow {}^4A_{2g}(F)$ and/or splitting of ^2G free ion term)	633
533	19762	$^4T_{1g}(F) \rightarrow {}^4T_{1g}(P)$	534
396	25253	$(^4T_{1g}(F) \rightarrow {}^2T_{1g}(H))$	395

Table S8. Band positions and assignment for DRUV spectrum of $Zn_{0.35}Co_{0.65}O$ on SPE at 0.9 V vs RHE in 1 M KOH in **Figure 4b**. The bands are assigned assuming octahedral Co^{2+} (d^7). Transitions are derived from Tanabe-Sugano diagram for d^7 octahedral (approximated values: B = 791 cm^{-1}, Δ/B = 10.7).

Wavelength	**Wavenumber**	**assigned transition**	**expected at**
[/nm]	[/cm^{-1}]		[/nm]
630	15873	$(^4T_{1g}(F) \rightarrow {}^4A_{2g}(F)$ and/or splitting of ^2G free ion term)	630
548	18248	$^4T_{1g}(F) \rightarrow {}^4T_{1g}(P)$	548
407	24570	$(^4T_{1g}(F) \rightarrow {}^2T_{1g}(H))$	407

Additional information on $CoAl_2O_4$

Figure S5 shows the Al2p, C1s and O1s XPS spectra. In **Figure S5a**, the main peak is that of the Al2p, the two other peaks at higher binding energies correspond to the Au $4f_{7/2}$ and $4f_{5/2}$ (at 84.0 eV and at 87.7 eV, respectively) and the rising intensity at lower binding energy is due to Co3p. In Fig. S5b), the C1s peaks in **Figure S5b** are shifted by 5.1 eV (before reaction) and 3.8 eV (after reaction) as compared to the expected energy for adventitious carbon (~284.8 eV) [2]. The O1s spectra in **Figure 5c** also shows high binding energy peaks, which match well the energy shifts observed for the C1s. In addition, we observed that the core level of all the elements, except for those of gold, were subject to rigid energy shifts to lower binding when reducing the X-ray intensity (not shown here) indicating that charging of the $CoAl_2O_4$ film occurs upon irradiation. Given that XPS is a surface sensitive technique, this further shows that part of the analyzed area includes uncovered gold patches. Consistently, to correct for the sample charging, rigid shifts of 5.1 eV and 3.8 eV were applied to the spectra before and after reaction, respectively. Note that this procedure was also applied to the Co spectra shown in the main text. With this, we obtain consistent binding energies for all the elements. After reaction, we remark minor rigid shifts of the Co2p, Al2p and O1s core level as mentioned in the main text, which are attributed to changes in the Fermi level.

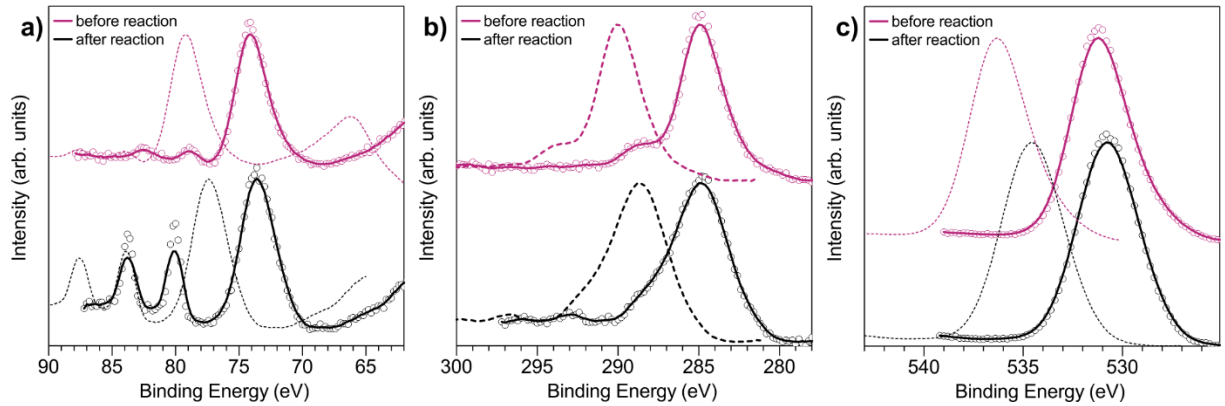

Figure S7. XPS spectra on a) the Al edge, b) the C edge and c) the O edge before and after 1 h electrochemical reaction at 10 $mAcm^{-2}$. Dashed lines represent the measured spectra, solid lines the corrected.

Table S9. EXAFS fit parameters at the Co-K edge for $CoAl_2O_4$ after electrochemical reaction. The amplitude reduction factor was fitted first from the Co-foil to reduce the number of variables.

				Path	*N*	*R*(Å)	σ²(Å²)	Δ*E* (eV)	±*R*(Å)	±σ²(Å²)	±Δ*E* (eV)
***R*-factor**	0.0235	N_{idp}	17.6	Co-O1	4	1.999	0.0053	2.831	0.012	0.0009	1.622
S_0^2	0.83195	N_{var}	11	Co-Al1	12	3.295	0.0135	-7.468	0.020	0.0015	2.020
***R*-range fit**	1.15 – 3.6	χ^2	863	Co-O2	12	3.331	0.0135	2.831	0.020	0.0015	1.622

***k*-range fit**	3.2 – 11.0	$\chi^2_{red.}$	132	Co-Co1	4	3.444	0.0135	-7.468	0.020	0.0015	2.020

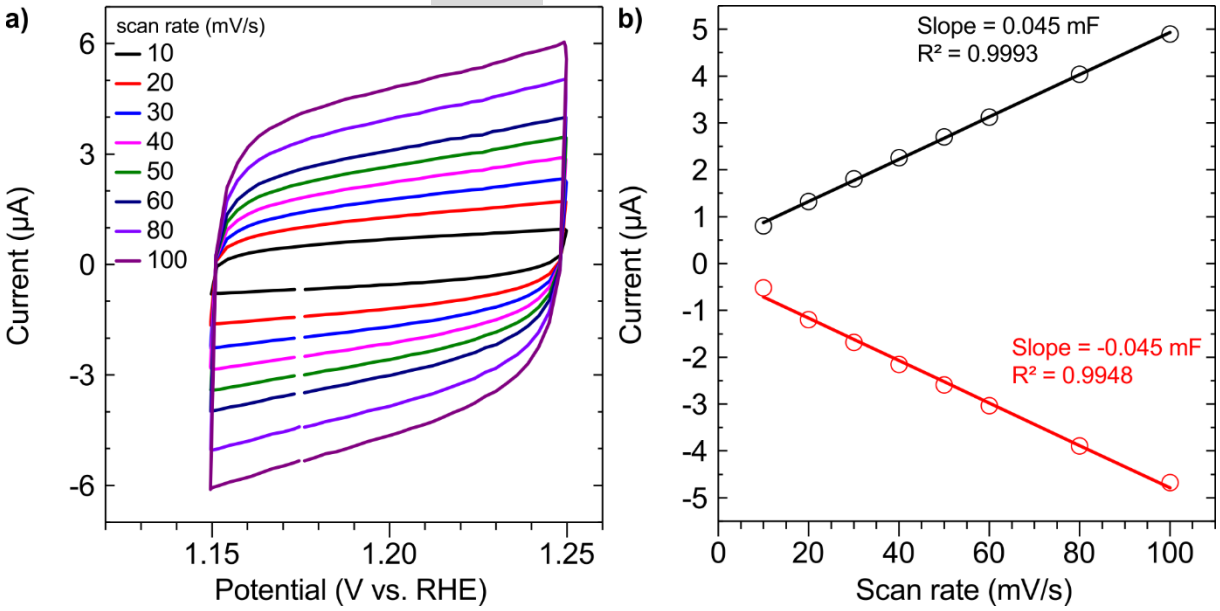

Figure S8. a) Double-layer capacitance (C_{dl}) measurements of $CoAl_2O_4$ for determining the electrochemically active surface area (*ECSA*) in 1 M KOH. 3rd cycle out of 5 cyclic voltammograms that were measured with different scan rates in the non-Faradaic region (100 mV potential window around 1.2 V vs RHE). b) The anodic (black) and cathodic (red) charging currents versus the scan rate. The data-points are the currents measured at 1.2 V, averaged over the last 4 CV cycles of each scan rate. The double-layer capacitance is calculated as the average of the absolute slopes of the linear fit. The values calculated are: C_{dl} = 0.045 mF, *ECSA* = 1.13 cm² and roughness R_f = 15.99.

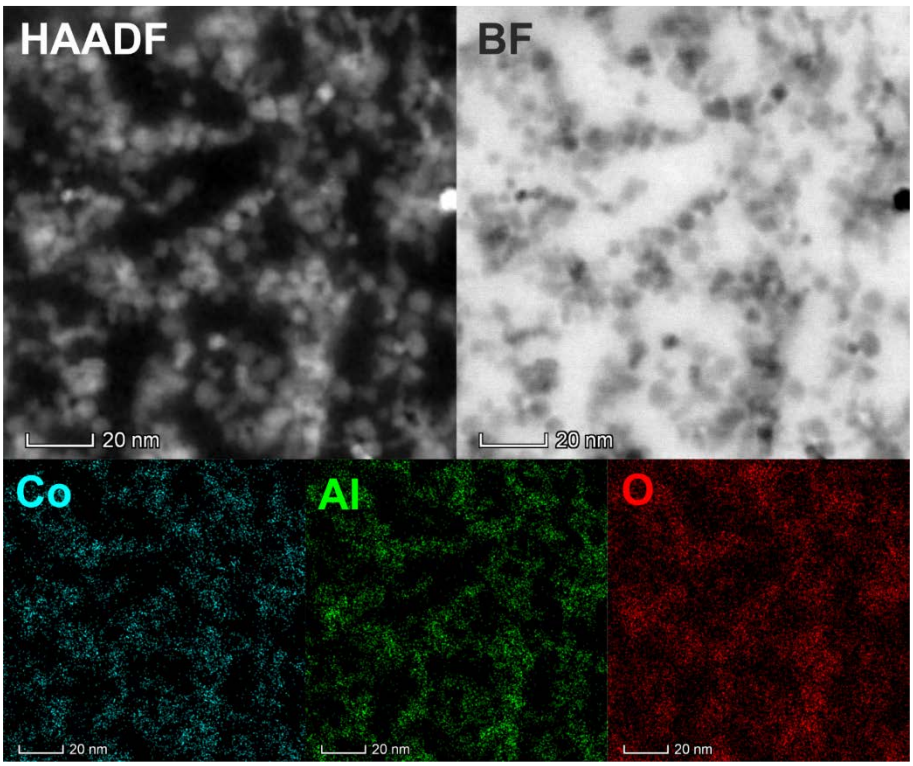

Figure S9. STEM HAADF and bright field micrographs and EDX mapping of cobalt, aluminum, and oxygen in $CoAl_2O_4$ before the reaction.

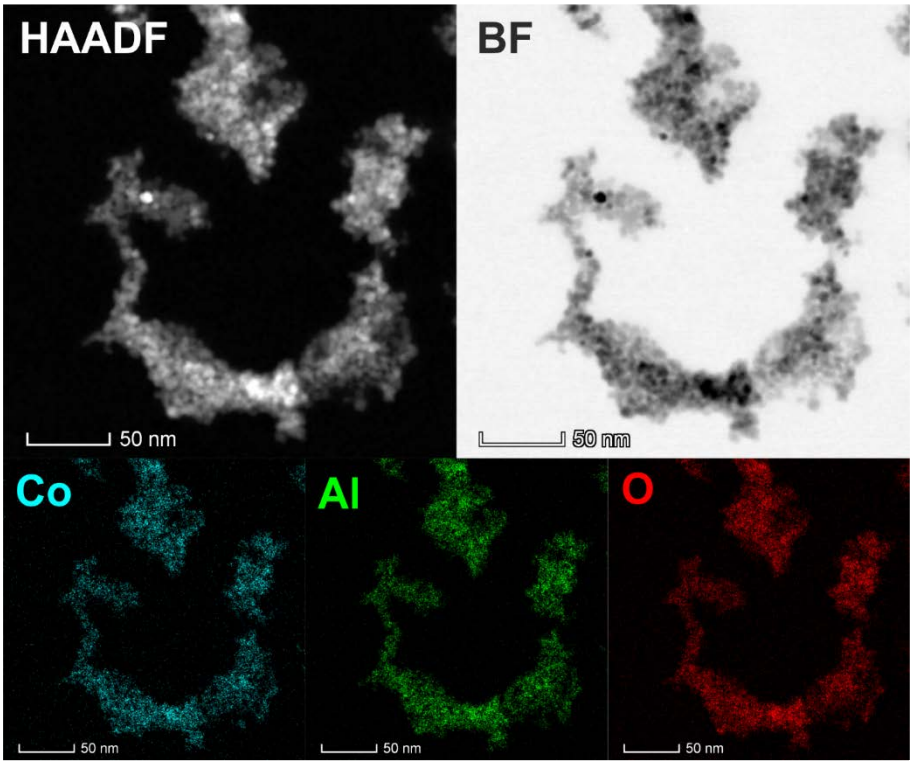

Figure S10. STEM HAADF and bright field micrographs and EDX mapping of cobalt, aluminum, and oxygen in $CoAl_2O_4$ after the reaction.

Calculation of aluminum atoms in top most nanoparticle shell

Following Lippens' and Lannoos equations 3a and 3b, the number N of atoms in a particle is related to the numbers of shells.[3] If we approximate a spherical shape for our particles, and take into account only the diameter of the largest (smallest) particles, which is 7.4 nm (4.6 nm), we can approximate a volume for one nanoparticle V_{NP} = 212,175 Å^3 (V_{NP} = 50,965 Å^3). Since the crystal structure is known, also the lattice parameter is known (a = 8.10670). From this the volume of a unit cell is V_{UC} = 532.76 Å^3. Furthermore, in a spinel, the unit cell is constructed of oxygen atoms in a face-centered cubic cell, i.e. in closed cubic packing. Thus, a unit cell contains 32 O, and 16 Al and 8 Co atoms in the octahedral and tetrahedral voids, respectively. Thus, the total number of O atoms can be derived from **Equation S1** to be n_O = 12744 (n_O = 3061). This corresponds, according to Lippens and Lannoo, to a particle consisting of 25 to 26 shells (15 to 16 shells). For 26 shells, 1564 atoms would be located in the top most shell (564 for 16 shells). Thus, ~11 % (~18 %) of all atoms are located in the top most shell.

$$n_O = 32 * \frac{V_{NP}}{V_{UC}} \quad \textbf{(S1)}$$

The EDX results in **Table 1** indicate an Al content of 60 %, which means a 10 % decrease compared to the perfect unit cell, where the Al content is 66.67 %. Thus, we can approximate, that all leached aluminum can origin from the top most layer.

Operando cells

The main design considerations for the SEC were based on minimizing the optical path to maximize the yield of reflected light. A large electrolyte reservoir was avoided by using a peristaltic pump flushing the cell with the electrolyte. By this, the evolving gases as well as dissolved species origin from the catalyst surface are carried away from the electrode. Thus, all measured activity can be assigned to the heterogeneous catalyst, and activity arising from homogeneous catalysts can be excluded. Despite of the low cell profile, a reversible hydrogen electrode (RHE) is used as the reference electrode. A schematic overview of the SEC can be found in Fig. S11 (see Experimental for detailed description and Fig. S12 for photographs).
As a proof of concept Fig. S1 shows two spectra taken with the same spectrophotometer configuration: $Zn_{0.35}Co_{0.65}O$ in powder form with a $BaSO_4$ background (a) and applied on the gold working electrode of an SPE with the bare electrode as background (b). The comparison shows an overall decreased intensity when measuring on the SPE, and a decrease in absorptions arising from Zn at lower and Co transitions at higher wavelengths. Although, the transitions of Co are clearly visible and show no energetic shift, and thus, an SPE with an Au WE is suitable to measure structural properties of cobalt containing samples.

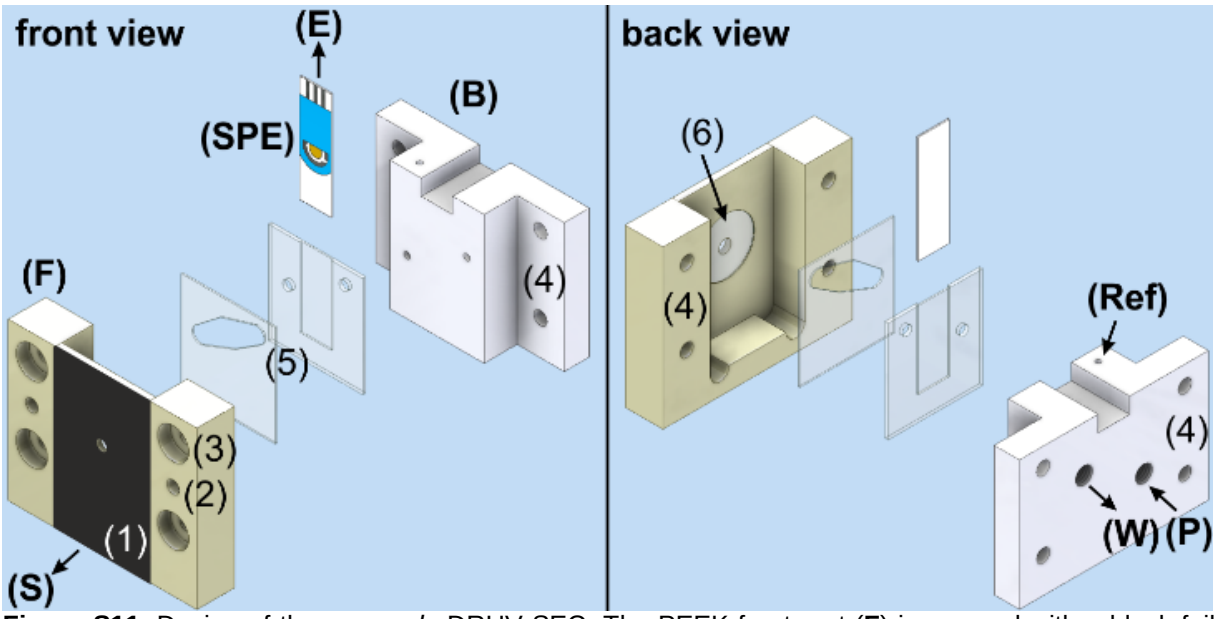

Figure S11. Design of the *operando* DRUV SEC. The PEEK front part (**F**) is covered with a black foil (1) and attached to the spectrophotometers (**S**) reflectance port by a mount and hold in place by magnets glued in cavities (2). The front is connected to the PTFE back (**B**) by nuts fixed in (3) and wing bolts going through holes (4). The electrode (**SPE**) is placed in the silicone gaskets (5) and connected to the potentiostat (**E**) by a connector cable. A Quartz window (6) is glued by silicone in a shallow cavity. The tip of the RHE reference electrode (**Ref**) is in contact to the electrolyte in the inlet channel. The electrolyte is flushed by a peristaltic pump (**P**) through PTFE tubes connected with HPLC fittings to the reservoir and the waste (**W**). A 3D-printed cover protects the setup from ambient light.

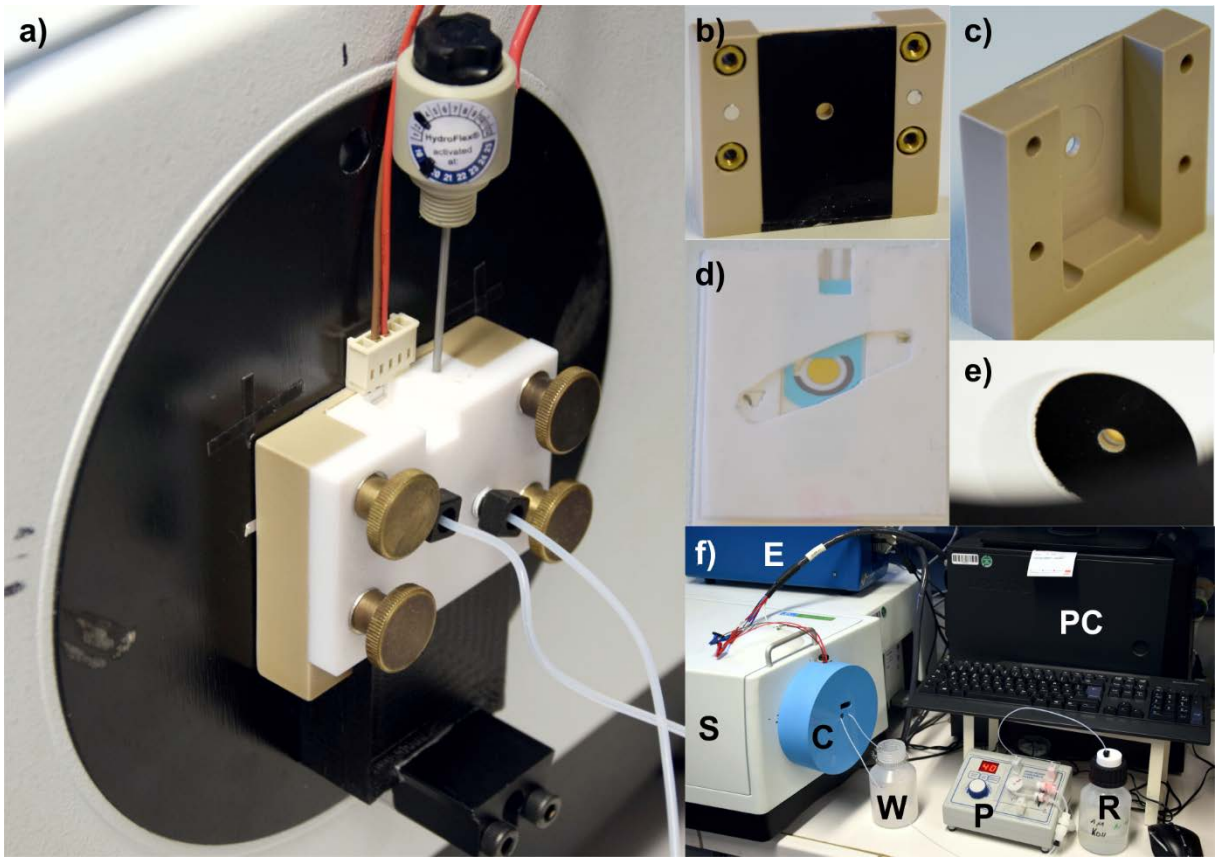

Figure S12. Photographs of the *operando* DRUV cell. a) Cell mounted at the reflectance port of the UV-vis spectrophotometer, equipped with the RHE. b) Front view of the PEEK part, covered with black absorbing foil. c) Back view of the PEEK part. d) Silicone gaskets and flow channel, equipped with the SPE. e) View in the integrating sphere showing the front of the cell and the Au working electrode. f) Full view of the setup. **S** is the UV-vis spectrophotometer, **E** is the potentiostat, **C** the 3D-printed cover. Through the cover go the electronic connections to the potentiostat and the tubes connecting the cell to the waste **W** and the peristaltic pump **P** that supplies the cell with electrolyte from the reservoir **R**. The spectrophotometer and the potentiostat are connected to the processing unit (**PC**).

Predecessor model of the cell.

The predecessor model of the *operando* cell used a plastic cuvette window instead of a Quartz window, limiting its wavelength range to the UV-visible. Instead of using silicone gaskets, a PTFE gasket was glued with silicone to the front part of the cell, to direct the flow of the electrolyte. The intention to redesign the cell was based on optimizing the flow of electrolyte as well as on making it more transferable to other kind of measurements, like *operando* X-ray absorption spectroscopy.

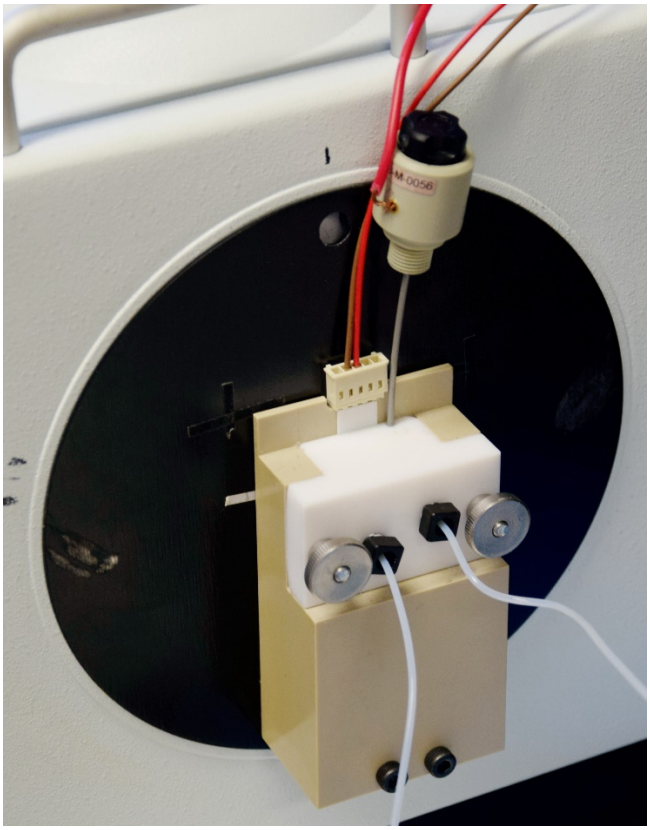

Figure S13. Photograph of the predecessor *operando* cell mounted on the reflectance port of the UV-vis spectrophotometer, equipped with the RHE and connected to the potentiostat, the pump and the waste.

References

1. Lancashire, R. J. Tanabe-Sugano diagrams via spreadsheets. http://wwwchem.uwimona.edu.jm/courses/Tanabe-Sugano/TSspread.html (accessed May 13, 2019).
2. Jacquemin, M.; Genet, M. J.; Gaigneaux, E. M.; Debecker, D. P. Calibration of the X-Ray Photoelectron Spectroscopy Binding Energy Scale for the Characterization of Heterogeneous Catalysts: Is Everything Really under Control? *ChemPhysChem* **2013,** *14* (15), 3618-3626.
3. Lippens, P. E.; Lannoo, M. Calculation of the band gap for small CdS and ZnS crystallites. *Physical review. B, Condensed matter* **1989,** *39* (15), 10935-10942.